The Meteoritical Society

Meteoritics & Planetary Science 1–27 (2025)
doi: 10.1111/maps.70069

Sulfur-bearing serpentine in carbonaceous chondrites

N. TOPPING[1]*, J. C. BRIDGES[1], L. J. HICKS[2], L. PETERA[3,4], C. S. ALLEN[5,6], J. RYU[5], D. G. HOPKINSON[5], M. DANAIE[5], L. BLASE[1,7], F. M. WILLCOCKS[1], G. DOUGLAS[8], H. G. CHANGELA[9,10], T. NOGUCHI[11], T. MATSUMOTO[11], and A. MIYAKE[11]

[1]School of Physics and Astronomy, University of Leicester, Leicester, UK
[2]School of Geology, Geography and the Environment, University of Leicester, Leicester, UK
[3]Department of Spectroscopy, J. Heyrovsky Institute of Physical Chemistry, Czech Academy of Sciences, Prague, Czechia
[4]Department of Inorganic Chemistry, Charles University Prague, Prague, Czechia
[5]Electron Physical Science Imaging Centre (ePSIC), Diamond Light Source, Harwell, UK
[6]Department of Materials, University of Oxford, Oxford, UK
[7]Department of Physical Sciences, University of Liverpool, Liverpool, UK
[8]School of Engineering, University of Leicester, Leicester, UK
[9]SETI Institute, Mountain View, California, USA
[10]Department of Earth and Planetary Science, University of New Mexico, Albuquerque, New Mexico, USA
[11]Division of Earth and Planetary Sciences, Kyoto University, Kyoto, Japan

***Correspondence**
N. Topping, School of Physics and Astronomy, University of Leicester, Leicester LE1 7RH, UK.
Email: nt229@leicester.ac.uk

(Received 21 March 2025; revision accepted 13 October 2025)

Abstract–A correlative multi-technique approach, including electron microscopy and X-ray synchrotron work, has been used to obtain both structural and compositional information of a sulfur-bearing serpentine identified in several carbonaceous chondrites (Winchcombe CM2, Aguas Zarcas CM2, Ivuna CI, and Orgueil CI), and in Ryugu samples returned by the Hayabusa2 mission. S-K edge X-ray absorption spectroscopy was used to determine the oxidation state of sulfur in the serpentine in all samples except Ryugu. The abundance of this phase varies across these samples, with the largest amount in Winchcombe; ~12 vol% of phyllosilicates are identified as sulfur-bearing serpentine characterized by ~10 wt% SO_3 equivalent. HRTEM studies reveal a d_{001}-spacing range of 0.64–0.70 nm across all sulfur-bearing serpentine sites, averaging 0.68 nm, characteristic of serpentine. Sulfur-serpentine has variable $S^{6+}/\Sigma S_{total}$ values and different sulfur species dependent on specimen type, with CM sulfur-bearing serpentine having values of 0.1–0.2 and S^{2-} as the dominant valency, and CIs having values of 0.9–1.0 with S^{6+} as the dominant valency. We suggest sulfur is structurally incorporated into serpentine as SH^- partially replacing OH^-, and trapped as SO_4^{2-} ions, with an approximate mineral formula of $(Mg\ Fe^{2+}\ Fe^{3+}\ Al)_{2\text{-}3}(Si\ Al)_2O_5(OH)_{5\text{-}6}(HS^-)_{1\text{-}2}(SO_4)^{2-}{}_{0.1\text{-}0.7}$. We conclude that much of the material identified in previous studies of carbonaceous chondrites as TCI-like or PCPs could be sulfur-bearing serpentine. The relatively high abundance of sulfur-bearing serpentine suggests that incorporation of sulfur into this phase was a significant part of the S-cycle in the early Solar System.

INTRODUCTION

It is accepted that carbonaceous chondrites (CCs) underwent extensive aqueous alteration on their parent bodies (Brearley, 2006; Suttle et al., 2021; Tomeoka & Buseck, 1988; Zolensky et al., 1993, 1997), producing secondary minerals. Alteration of olivine and pyroxene created abundant serpentine and saponite

(Brearley, 2006; Howard et al., 2009; Suttle et al., 2021; Tomeoka & Buseck, 1988; Zolensky et al., 1993). It is these altered minerals, with water and other volatiles trapped within their structures, which can be studied to better understand the transport and distribution of water and volatile elements in the Solar System, including sulfur. Both the Mighei-type (CM) and Ivuna-type (CI) chondrites are considered to contain the most extensive evidence of aqueous alteration (Bunch & Chang, 1980), where the resulting materials are phyllosilicate-rich matrices. Phyllosilicates are the most abundant mineral across CCs (Brearley & Jones, 1998), with around 80% volume in both the CM and CI chondrites (Garvie, 2021; Ito et al., 2022; King et al., 2015, 2022). Analyses of samples from C-class asteroids Ryugu and Bennu, returned by Hayabusa2 and OSIRIS-REx, respectively, also find phyllosilicate abundance of ~78% in Ryugu (Ito et al., 2022; Yamaguchi et al., 2023) and ~80% in Bennu (King et al., 2024), as expected from studies for CI chondrites. The dominant phyllosilicate mineral phase is serpentine-like material (Bates et al., 2020; Buseck & Hua, 1993; McSween, 1987).

Serpentine, $(Mg, Fe, Al)_{2-}$ Si O (OH) , is a sheet silicate with a structure that is built around a repeating unit of tetrahedral and octahedral (T-O) site occupancy layers in a 1:1 ratio, and a (0 0 1) basal plane spacing of ~0.70 nm (Hicks et al., 2014; Zega et al., 2006) (Figure 1). The tetrahedral sites have fourfold coordination, meaning that there are four anions bonded to the central cation, forming a tetrahedron. Similarly, the octahedral sites have sixfold coordination, with six anions bonded to the central cation, outlining an octahedron. The linked SiO_4 tetrahedra form a pseudo-hexagonal layer, with all tetrahedra pointing in the same direction. A brucite-like, $Mg(OH)_2$, layer is joined to the tetrahedral sheet on one side, where two out of the three hydroxyls are replaced by apical oxygens of the SiO_4 tetrahedra (Deer et al., 1992). In serpentine, common substitutions occur in the cation sites, in the form of Al^{3+} partially replacing Si^{4+}, and Fe^{3+} substituting for Al^{4+} and Si^{4+} in the tetrahedra, and Fe^{3+} and Al^{3+} substituting for Mg^{2+} in the octahedra. Despite the physical and chemical structure of serpentine in CCs being widely studied (e.g., Bischoff, 1998; King et al., 2015, 2017; Velbel & Palmer, 2011), ongoing work aims to further understand its complexities and the formation and significance of these secondary minerals in primitive meteorites. To date, there has been little recognition of the role of sulfur in extraterrestrial serpentine formation, with the exception of Zega et al. (2004).

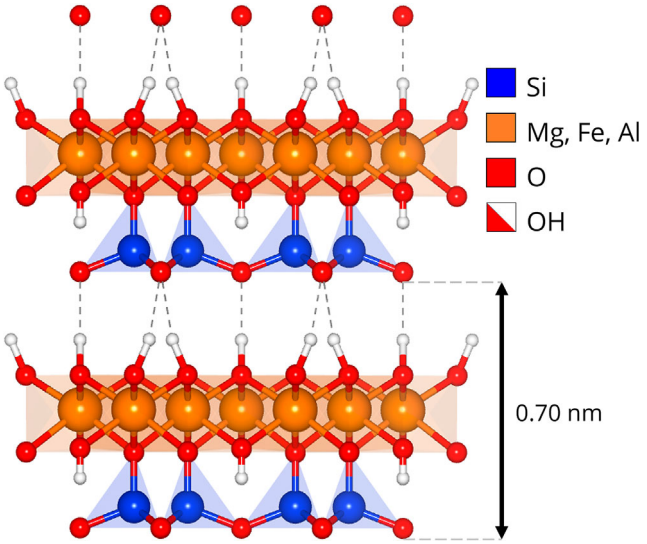

FIGURE 1. Schematic of the structure of serpentine showing four unit cells. The tetrahedral and octahedral layers are represented by blue triangles and orange squares, respectively. The dashed vertical lines show the interlayer forces. The lattice spacing for serpentine is 0.70 nm. Created using VESTA 3 (v 3.5.8) modeling software (Momma & Izumi, 2011).

Sulfur in CCs

Sulfur is the tenth most abundant element in the Solar System (Räisänen, 2005). It can take on a wide range of oxidation states from S^{2-} to S^{6+} and is present as various chemical forms in both terrestrial and extraterrestrial samples (Naraoka et al., 2023). Sulfur is significant as it is a geochemically, mineralogically, and biologically important element; it is one of the essential elements for life in forming amino acids, the building blocks of proteins (Brosnan & Brosnan, 2006; Sievert et al., 2007), and in the biogeochemical cycling of sulfur (Charlson et al., 2000; Jørgensen et al., 2019). Owing to its unique range of valence states, sulfur is a key indicator of redox conditions on parent bodies. Iron-sulfide is ubiquitous across all chondrites (Schrader et al., 2021), largely in the form of pyrrhotite ($Fe_{1-x}{}^{2+}S^{2-}$) and troilite ($Fe^{2+}S^{2-}$) and has been used as an indicator of formation and alteration of small Solar System bodies by analyzing the Fe to S ratios (Schrader et al., 2016; Singerling & Brearley, 2020). Studying the mineralogical aspects of the sulfur cycle offers insights into water-rock reaction history on chondrite parent bodies and the sulfur cycle in the early Solar System.

Several types of sulfur-bearing minerals (e.g., sulfides, sulfates, tochilinite) are found in CCs (Bullock et al., 2010) and abundance varies across CC types; the CMs contain ~1.7–3.4 wt% sulfur and the CIs contain ~3.0–4.4 wt% sulfur (Burgess et al., 1991), with sulfide abundances of

0.6–5.4 vol% in the CMs (Howard et al., 2015) and 2.2–7.0 vol% in the CIs (King et al., 2015). For the samples used in this study, Winchcombe has bulk sulfur content of ~3.2 wt% (Bates et al., 2024), Aguas Zarcas ~2.7 wt% (Arai et al., 2022), Ivuna ~4.8 wt% (Alexander et al., 2022; Braukmüller et al., 2018, 2019; Burgess et al., 1991; Dreibus et al., 1995), Orgueil ~4.6 wt% (Alexander et al., 2022; Braukmüller et al., 2018, 2019; Burgess et al., 1991; Dreibus et al., 1995), and Ryugu ~4.4 wt% (chamber A samples, designated surface samples, Tachibana et al., 2022) and ~5.9 wt% (chamber C samples, designated subsurface samples, Tachibana et al., 2022) (Nakamura et al., 2022; Yokoyama et al., 2023; Yoshimura et al., 2023). Thus Winchcombe does not have a bulk enrichment in sulfur relative to other CCs.

During alteration on the earliest carbonaceous parent bodies, amorphous silicate matrices, metals and sulfides were aqueously altered to form Fe-Ni-S-rich phases along with magnetite, secondary sulfides and carbonates (calcite and, more rarely, dolomite). Originally termed "poorly characterized phases" (PCPs) by Fuchs et al. (1973) due to their complex mineralogy, these Fe, S-rich alteration products are now often described as tochilinite-cronstedtite intergrowths (TCIs) after work by Mackinnon and Zolensky (1984). Tochilinite ($Fe^{2+}{}_{5–6}(Mg, Fe^{2+})_5S_6(OH)_{10}$) is a hydrated Fe-sulfide and cronstedtite ($Fe^{2+}{}_2Fe^{3+}(Si, Fe^{3+})O_5)(OH)_4$) is an Fe-rich serpentine-like mineral. Since then, the term TCI has been used as a descriptor of various Fe, S-alteration phases in CM chondrites (Daly et al., 2024; McSween, 1987; Pignatelli et al., 2017; Rubin et al., 2007; Tomeoka & Buseck, 1985; Vacher et al., 2019) which are characterized by a fibrous, acicular Fe, S-rich rim around Mg-rich phyllosilicate cores, carbonates or void space.

TCIs are broadly categorized into two types; type I TCIs are predominantly tochilinite with minor abundances of cronstedtite and magnetite and mostly occur in chondrules as large, rounded forms (Nakamura & Nakamuta, 1996; Pignatelli et al., 2016). Conversely, type II TCIs have fibrous textures and occur most commonly in the matrix, where cronstedtite is the dominant phase and tochilinite is also present, alongside a mixed-layer mineral made up of both cronstedtite and tochilinite (Pignatelli et al., 2016; Suttle et al., 2021). Though several pathways have been suggested for the formation of both type I and type II TCIs (e.g., Lee & Greenwood, 1994; Lee et al., 2013; Nakamura & Nakamuta, 1996; Tomeoka & Buseck, 1985), their occurrence and exact mineralogy is poorly understood.

These sulfur-bearing minerals can, however, provide insights into the distribution and retention of sulfur during planetary formation, temperatures, fluid composition and timescales of alteration on CC parent bodies.

The presence of sulfur in serpentine in terrestrial materials has previously been studied by Debret et al. (2017), investigating the role of abyssal serpentine minerals as sulfur carriers via microscale X-ray absorption near-edge structure (μ-XANES), secondary ion mass spectrometry (SIMS) analyses and X-ray fluorescence (XRF) mapping. In these phases, the occurrence of sulfur is associated with the crystallization of sulfur-bearing minerals, notably sulfides and sulfates; however, Debret et al. (2017) concluded that sulfur (in the form of S^{6+} ions) is structurally incorporated into the serpentine mineral structure. Zega et al. (2004) have previously reported the inclusion of sulfur in serpentine-like nanotubes in the Mighei CM chondrite, identified using high-resolution transmission electron microscopy (HRTEM) imaging and electron energy-loss spectroscopy (EELS) analyses, noting that the Fe, S-rich composition is different to other meteoritic and terrestrial mineral phases, and suggest this to be a new type of serpentine. Based on the existence of a sulfur-bearing mica and the homogenous distribution of sulfur in these phases, Zega et al. (2004) suggested that sulfur is a structural component of serpentine, substituting O^{2-} ions with S^{2-}. This idea has been referenced more recently in the Garvie (2021) study of the CM chondrite Aguas Zarcas. S-bearing phyllosilicate in Aguas Zarcas was attributed to "unresolved sub-micrometer sulfides" in the phyllosilicates, but the author also suggests sulfur may be structurally incorporated into the serpentine, based on the work of Zega et al. (2004). However, Garvie (2021) does note that SEM-scale analyses do not have the required high-spatial resolution needed to resolve individual phases (micrometer to sub-micrometer) that constitute the matrix mineralogy.

Building upon the findings of Zega et al. (2004), Debret et al. (2017) and Garvie (2021), we have adopted a correlative, multi-technique approach combining electron microscopy and X-ray absorption near-edge spectroscopy (XANES) across a range of CM- and CI-type samples to better understand a potential link between serpentine formation, the sulfur cycle and related redox conditions on CC parent bodies. As phyllosilicates constitute ~80 vol% of CM chondrites, and if sulfur constitutes at least a minor fraction of their chemical composition, then phyllosilicates may have a significant role in the sulfur cycle and distribution of volatiles in the early Solar System. We note that 2:1 and 1:1 mix-layered phyllosilicates (saponite-serpentine) have been identified in Ryugu (Changela et al., 2024; Ito et al., 2022); however, the focus of this study is on 1:1 serpentine, which is the most abundant phyllosilicate.

MATERIALS AND METHODS

Five CCs have been studied as polished thin sections, polished resin blocks and lamellae suitable for use in transmission electron microscopy (TEM): Winchcombe CM2 (NHM section P30543), Aguas Zarcas CM2 (U. Leicester), Ivuna CI1 (NHM section P12628), Orgueil CI1 (NHM section P16061) and Ryugu lamellae (samples C0105-035_000_00, A0058-C2001_08, A0104-017_006_02) from the JAXA Hayabusa2 sample return mission.

Sample thin sections and blocks were studied and characterized using back scattered electron (BSE) imaging and energy dispersive X-ray spectroscopy (EDS) using a FEG-SEM (FEI Quanta 650) equipped with a silicon drift EDS detector (Oxford Instruments (OI) 20 mm^2 X-MaxN) at the University of Leicester (UoL) Advanced Microscopy Facility (AMF). EDS spectra were measured with an accelerating voltage of 15 kV and spot size 5 (beam current ~1 nA) and analyzed using OI AZtec software (v. 6.0).

Standardized, "quant-optimized" EDS for unnormalized compositional measurements was performed using a FIB-SEM (Zeiss Crossbeam 350) equipped with a silicon drift EDS detector (OI 100 mm^2 UltimMax) at the Hercules Facility (UoL AMF). Data was collected with an accelerating voltage of 15 kV and beam current ~3.5 nA. The following standards were used (MAC mineral block no. 11582): albite (Na), labradorite (Al), pyrite (S), orthoclase (K), wollastonite (Ca), ilmenite (Ti), chromite (Cr), rhodochrosite (Mn), and olivine (Fe). Factory standards, supplied by OI in AZtec, were used for two elements; magnesium oxide (Mg) and silicon dioxide (Si).

TEM lamellae of approximate dimensions 5 µm × 15 µm and ≤ 100 nm thickness were prepared using standard lift-out procedures (Daly et al., 2020; Hicks, 2015; Lee et al., 2003) on the following instruments; FEI Quanta 200 3D Dual FIB-SEM (UoL AMF), and a Zeiss Crossbeam 350 FIB-SEM (Hercules Facility, UoL AMF). One Ivuna lamella was prepared using a Helios 5 Hydra DualBeam FIB-SEM at CEITIC, Masaryk University, Czechia (Petera et al., 2023). Ryugu samples A0058-C2001_08 and A0104-017_006_02 were prepared using a ThermoFisher Helios FIB-SEM at Kyoto University (Noguchi et al., 2023).

Scanning transmission electron microscopy (STEM) data for Winchcombe, Aguas Zargas, Ivuna and Ryugu lamellae were collected using aberration-corrected TEM; a JEOL ARM200CF (E01 from herein) and JEOL ARM300CF (E02 from herein) at the electron Physical Science Imaging Centre (ePSIC) of Diamond Light Source (DLS), UK. STEM-EDS was obtained via E01, and HRTEM imaging for lattice spacing measurements, and four-dimensional-STEM (4D STEM) with correlative EDS were collected using E02. Additional non–aberration-corrected HRTEM imaging was performed on a JEOL 2100 TEM at UoL AMF (Winchcombe only), with further HRTEM and EDS performed on a JEOL 2100+ TEM at the University of Nottingham nanoscale and microscale Research Centre (UoN nmRC) on Ryugu A0058-C2001_08 only. E01 EDS measurements were carried out at an accelerating voltage of 200 kV and beam current 41 pA, with step sizes between 6 and 20 nm dependent on the size of the site of interest. The following standards were used to determine the experimental k-factors used in the analysis of the STEM-EDS data; San Carlos olivine, pyroxene within Winchcombe, Aguas Zarcas and Ivuna lamella, and olivine from a Martian nakhlite (NWA 15364). EDS data were analyzed using the Hyperspy (v2.0.1) package in Python (de la Peña et al., 2024). E02 HRTEM imaging and lattice measurements were carried out at an accelerating voltage of 200 kV (Ivuna only) and 300 kV and beam currents 28 pA and 25 pA, respectively. These were calibrated using a gold standard (gold nanoparticles deposited on a carbon substrate) with known distance of 0.1442 nm for the (2 2 0) reflection of gold. Lattice measurements were made using the open-source image processing software ImageJ (Schneider et al., 2012).

Nanobeam 4D STEM and correlative EDS were collected for Winchcombe only. Unlike conventional STEM where scattered electrons falling into a specific range of collection angles are recorded as the electron beam is rastered over a sample, in 4D STEM a 2D diffraction pattern is collected at every (2D) probe position, producing a 4D dataset (Ophus, 2019, 2023). This technique is enhanced further by combining with EDS, resulting in a dataset with spatially correlated compositional (EDS) and crystallographic (4D STEM) information. Measurements were acquired with an accelerating voltage of 300 kV, beam current 7.6 pA, step sizes of ~2.9–7.4 nm, convergence semi-angles ~0.3 mrad, and each site of interest was scanned twice with dwell times 1–8 ms and camera lengths (CL) 40 and 100 cm. A gold standard was used for calibration of the microscope and the data. 4D STEM datasets were analyzed in Python using the open-source py4DSTEM package (Savitzky et al., 2021) and EDS using the Hyperspy package (de la Peña et al., 2024). To clearly analyze Bragg peaks that were produced from a mixed-phase material or small crystals, each 2D diffraction pattern was transformed into a 1D radial variance profile. The 3D (scan x and y dimensions, and 1D profile) radial variance profile dataset was decomposed using non-negative matrix factorization (NMF) to extract important features from the dataset and visualize their distribution across the scan area (Ryu et al., 2021; Uesugi et al., 2021). The NMF analysis decomposes the radial profile dataset into a linear combination of loading vectors that represent a strong Bragg reflection component in the dataset. Using this approach, the 4D STEM data were segmented into

several groups, each corresponding to strong Bragg reflections. The dataset presented here was segmented using 20 loading vectors. More details on the method used can be found in the Supporting Information S3.

To analyze the oxidation state of sulfur, X-ray absorption near-edge structure (XANES) measurements were collected on the I18 microfocus beamline at DLS synchrotron, with 2 μm resolution. XRF mapping of the site of interest was first carried out on elements Fe and S, to clearly identify the analysis regions, followed by S-K edge XANES. Samples analyzed were Winchcombe, Ivuna, Orgueil (polished blocks) and Aguas Zarcas (thin section) and several standard reference materials: native sulfur (S^0), pyrite (FeS_2; S^{1-}), chalcopyrite ($CuFeS_2$; S^{2-}), sphalerite ((Zn, Fe)S; S^{2-}), barite ($BaSO_4$; S^{6+}), magnesium sulfate ($MgSO_4$; S^{6+}), anhydrite ($CaSO_4$; S^{6+}) and gypsum ($CaSO_4{\cdot}2H_2O$; S^{6+}). All were measured in fluorescence mode at 45° to the beam and the detector. For the standards, native sulfur, pyrite and magnesium sulfate, were all powders, while a MAC (no. 11582) mineral standards block was used for the remaining standards. All measurements were taken over an energy range 2450–3000 eV, with varying energy resolutions; 0.5 eV in the pre-edge region (2450–2464 eV), 0.2 eV in the edge region (2464–2484 eV), 0.5 eV in the post-edge region (2484–2500 kV) and 1.0 and 5.0 eV for the ranges 2500–2520 eV and 2520–2000 eV, respectively. Data were acquired with 1 s acquisition time per energy step. The XANES data were processed and normalized in the open-source software Athena 0.9.26 (Anzures et al., 2020; Ravel & Newville, 2005). All spectra were calibrated against elemental sulfur by measuring the derivative of the S^0 absorption edge in Athena and correcting to $E_0 = 2472$ eV. Absorption edge energies were measured as the energy of the normalized spectra at an intensity of 0.5 (a.u). Spectra were summed for each phase identified in each meteoritic sample, in order to improve the signal to noise ratio of the spectra to better identify the characteristic peaks of the different sulfur species, and to show the average S-K edge XANES spectra for the different sulfur-bearing serpentine phases. Approximate $S^{6+}/\Sigma S$ ratios were determined via linear combination fitting (LCF) of the standard spectra to the "unknown" spectra. Here, the maximum number of standards chosen for the fit was two. The LCF finds the most suitable ratio of the two standard spectra that best represent the unknown spectrum, thus allowing an approximate ratio of each sulfur species to be determined.

Fe-K edge XANES measurements were collected on Winchcombe to determine the ferric-ferrous ratio ($Fe^{3+}/\Sigma Fe$) of the serpentine phases. These measurements were collected at beamline I18 at DLS, over an energy range 7000–7500 eV, with the highest resolution step size of 0.1 eV in the edge region between 7105 and 7125 eV. Data were also processed and analyzed using Athena 0.9.26 (Ravel & Newville, 2005). More details on Fe-K XANES are in Supplementary Information S1.

RESULTS

Textures and Occurrence of S-bearing Serpentine

Serpentine-dominant regions were identified in the samples using SEM-BSE imaging, and initial, qualitative identification of sulfur-bearing serpentines using SEM-EDS normalized to 100 wt% anhydrous totals. Based on these initial findings, we classified the sulfur-bearing serpentines into three categories: S-poor, <1.0 wt% SO_3; S-bearing, 1.0–10.0 wt% SO_3; and S-rich, ≥ 10.0 wt% SO_3. Sulfur abundances are reported as SO_3 wt% equivalent, in order for ease of comparison to the literature (with the exception of Table 1 where results from the S-K edge XANES analyses have been applied). The relative abundance of the S-bearing and S-rich serpentine in Winchcombe is approximately 15 vol% of the total phyllosilicate present and ~12 vol% of the whole Winchcombe mineral assemblages. In our study, we seek to distinguish between S-bearing serpentine and "TCI-like objects" (Daly et al., 2024; Kerraouch et al., 2021; Suttle et al., 2024) (e.g., see Figure 3e "TCI-object"). This is considered further in the discussion. We describe the groundmass, which hosts the serpentine morphologies described below and the TCI-like objects as the matrix; it is a heterogenous mix of both coarse and fine-grained materials, and both anhydrous and altered minerals (Metzler et al., 1992). For the CIs, this groundmass is also called matrix, but it is noted that the CI matrix is more homogenous and has no TCI-like objects and few-to-no chondrules and clasts.

In Winchcombe, the serpentine regions are typically present as ~50 μm discrete domains, but with a range of sizes and shapes, and having a characteristic zoned appearance in BSE images, where the S-rich serpentines appear as lighter gray consistent with a higher average atomic number, compared to the darker gray S-bearing and S-poor serpentines. Both S-bearing and S-rich serpentine grow radially outwards from different nucleation sites and have fibrous, radiating textures (Figure 3a, labeled "S-Sp"). A common feature across all three sites is a lack of distinct tochilinite filaments. Characteristic serpentine morphology is shown in Figure 3a,b, and in the case of Figure 3a, intergrown with a 40 μm calcite grain.

Winchcombe sulfides are predominantly pentlandite, $(Ni, Fe)_9S_8$, with 30–35 wt% Ni, occurring as large subhedral grains up to 50 μm in size (Figure 4a). One

TABLE 1. Standardized, quant-optimized SEM-EDS compositions of representative serpentine and S-bearing serpentine phases.

	Winchcombe		Aguas Zarcas		Ivuna	
	S-bearing Serpentine	S-rich Serpentine	S-bearing Serpentine	S-rich Serpentine	Serpentine	S-rich Serpentine
n	12	6	3	3	3	4
SiO_2	25.1 (2.0)	15.7 (4.3)	25.8 (0.1)	16.1 (6.0)	40.0 (0.9)	21.1 (1.7)
TiO	-	-	-	-	-	-
Al_2O_3	3.4 (0.6)	1.6 (0.8)	2.3 (0.1)	2.5 (0.2)	8.7 (0.5)	2.6 (0.3)
Fe_2O_3	18.8 (1.6)	22.7 (3.8)	20.1 (0.3)	26.7 (5.7)	6.5 (0.1)	20.8 (2.5)
FeO	6.4 (0.5)	11.1 (2.4)	6.8 (0.1)	13.0 (2.8)	2.2 (0.1)	10.1 (1.2)
Cr_2O_3	-	-	-	0.2 (0.1)	0.8 (0.4)	0.9 (0.2)
NiO	1.0 (0.3)	1.6 (0.3)	1.1 (0.1)	2.1 (0.4)	-	2.0 (0.3)
MnO	-	-	-	0.2 (0.1)	-	-
MgO	21.5 (1.7)	13.8 (4.6)	19.6 (0.1)	13.8 (4.7)	22.1 (0.6)	8.0 (1.1)
CaO	-	0.1 (0.1)	-	0.1 (0.1)	-	-
Na_2O	1.4 (0.6)	-	0.7 (0.1)	-	-	-
K_2O	0.2 (0.1)	-	0.2 (0.1)	0.2 (0.1)	-	0.3 (0.1)
$(SO_4)^{2-}$	1.9 (0.5)	3.7 (0.7)	0.9 (0.1)	2.0 (0.5)	-	17.6 (3.2)
HS^-	7.7 (2.0)	14.9 (2.7)	7.7 (0.3)	18.0 (4.5)	-	1.1 (0.2)
Total	87.3	85.1	85.3	94.9	80.3	84.6
H_2O^+	12.7 (2.7)	14.9 (1.4)	14.8 (0.6)	5.1 (3.2)	19.7 (0.4)	15.4 (0.9)
$Fe^{3+}/\Sigma Fe$	0.57 ± 0.04	0.48 ± 0.04	0.57 ± 0.04	0.48 ± 0.04	0.57 ± 0.04	0.48 ± 0.04
$S^{6+}/\Sigma S$	0.19 ± 0.02	0.19 ± 0.02	0.10 ± 0.02	0.10 ± 0.02	-	0.94 ± 0.02
Mg#	72.1	53.6	68.7	49.6	88.5	42.4
(SO_3 equiv.)*	8.0 (2.1)	15.6 (2.9)	7.2 (0.3)	16.7 (4.1)	(-)	15.6 (2.7)
Number of ions on the basis of 9 (O, OH)[1]						
Si	1.32	0.87	1.34	1.08	1.76	1.00
^4Al	0.21	2.00 0.10	1.91 0.14	2.00 0.19	2.00 0.24	2.00 0.15	1.89
Fe^{3+}	0.47	0.94	0.52	0.73	-	0.74
^6Al	-	-	-	-	0.22	-
Fe^{3+}	0.27	-	0.27	0.62	0.22	-
Fe^{2+}	0.28	0.51	0.30	0.73	0.08	0.40
Mg	1.68	1.13	1.52	1.38	1.45	0.57
Cr	-	2.44 -	1.71 -	2.21 0.01	2.89 0.03	1.99 0.03	0.98
Ni	0.04	0.07	0.05	0.11	-	0.08
Mn	-	-	-	0.01	-	-
Ca	-	-	-	0.01	-	-
Na	0.15	-	0.07	-	-	-
K	0.01	-	0.01	0.02	-	0.02
OH^-	4.47	5.50	5.11	2.26	5.80	4.86
HS^-	0.74	1.51	0.73	2.19	-	0.10
$(SO_4)^{2-}$	0.06	0.12	0.03	0.08	-	0.52

Note: Quant-optimized SEM-EDS collected on Zeiss Crossbeam FIB-SEM at AMF, UoL. *n* is the number of analyses and values in parentheses are 1σ. A description of the calculation of H_2O by difference is provided in the Supporting Information. Sulfur abundances are reported as HS^- and $(SO_4)^{2-}$ equivalent, to correspond with the sulfur species identified via S-K edge XANES in S-K and Fe-K XANES Analyses Section and in order to determine a suitable mineral formula for the sulfur-bearing serpentine phase.

[a]Raw data SO_3 equivalent reported for ease of comparison to our definitions of S-bearing serpentine types and for comparison to the literature.

[b]Deer et al. (1992).

small cluster (<10, each grain approximately 10 μm) of pyrrhotite grains, $Fe_{1-x}S$, was also identified in the section under study. Some pentlandite grains show evidence of partial alteration to phyllosilicate, where the remaining sulfide is in direct contact with the new phyllosilicate phase. Nearly all sulfides occur as isolated grains as part of the clastic matrix, with the exception of some thin Fe, Ni, S-rich rims around chondrules. The carbonates identified are largely calcite in composition; however, some occurrences of dolomite have also been found (Suttle et al., 2024; this work).

In Aguas Zarcas, coarse-grained phyllosilicates appear as characteristic "clumps" such as Figure 3e, with dark Mg-rich serpentine cores (20–30 μm) and bright Fe-rich rims, and are the dominant textural type in this sample. There are TCI-like acicular filaments present at core edges, as well as being surrounded by an Fe, S-rich phyllosilicate-like ("TCI-like") phase at the rim. Most of the serpentines in these morphologies are S-poor or S-bearing, but there is some occurrence of small, radial growths of S-rich serpentine at core edges or in core centers, similar to those in Figure 3a. Figure 3d of Aguas Zarcas shows alteration of a relict chondrule to phyllosilicate, with pyroxene fragments (~10–20 μm) and an Fe, Ni sulfide rim.

Pentlandite (up to 35 wt% Ni) is the dominant sulfide species in Aguas Zarcas and occurs as large (up to 200 μm) isolated grains (Figure 4b). One large 300 μm chondrule is enclosed by a 20 μm thick Fe, Ni-rich sulfide rim with micrometer-sized Fe-sulfides within the brecciated anhydrous silicates in the chondrule. The largest sulfide in Aguas Zarcas

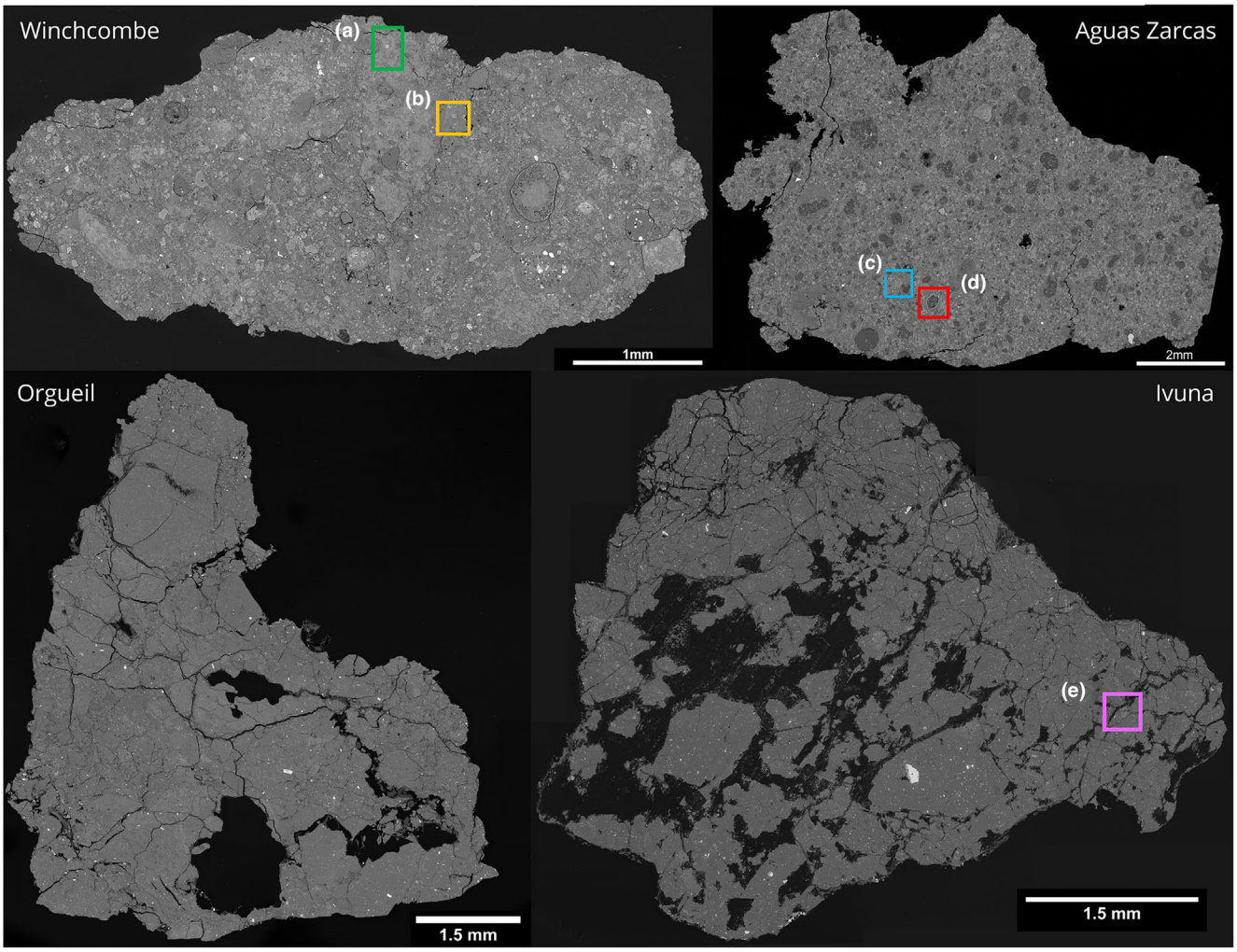

FIGURE 2. BSE images of the CM and the CI chondrites used in our study of S-bearing serpentine. Top row, L-R: CMs, Winchcombe and Aguas Zarcas. Bottom row, L-R: CIs, Orgueil and Ivuna. Winchcombe and Aguas Zarcas (CMs) have predominantly clastic matrix, with some fine-grained materials around chondrules and other inclusions. Ivuna and Orgueil have typically fine-grained homogeneous matrix with few-to-no chondrules or remnant anhydrous phases. Regions labeled A–F highlight where TEM lamellae were taken from sites of sulfur-bearing serpentine.

(~200 μm) is an Fe, S-rich sulfide, with alteration to phyllosilicate-like material at its center and 10 μm-sized grains of an Fe, Ni, S-rich sulfide with traces of P and K (4 wt% and <1 wt%, respectively), which are also present at the edges of this large grain. It is in direct contact with both altered and unaltered anhydrous silicate grains and appears to be in the center of what was once a chondrule.

Unlike the CMs, the CIs Ivuna and Orgueil have a near-homogeneous distribution of phyllosilicate materials, predominantly as fine-grained matrix (FGM) with little-to-no coarse-grained, distinct serpentine morphologies and an absence of phyllosilicate clumps and TCI-like objects. The phyllosilicates in the CIs (Figure 3f–h) mostly occur as dark FGM with framboidal and plaquette magnetite morphologies embedded within the FGM, along with sulfides and minor amounts of carbonate. Instances of coarse-grained serpentine fragments are rare across Ivuna and Orgueil; however, one near-circular fragment of serpentine (~40 μm diameter) was found in Ivuna (Figure 3g) with the coarse-grained fibrous texture visible at the microscale.

The sulfides occur as large (up to 40–50 μm) isolated hexagonal grains and lathes of low-Ni bearing pyrrhotite, $Fe_{1-x}S$, within the FGM (Figure 4). No pentlandite was found in these samples. Some of the sulfide grains have been partially corroded due to aqueous alteration, where phyllosilicates and some sulfates have started to form. In many cases, there is clear alteration of sulfides to form magnetites, where traces of the primary sulfide are found adjacent to framboidal magnetites. Large sulfides are more readily found in the CIs compared to the CMs.

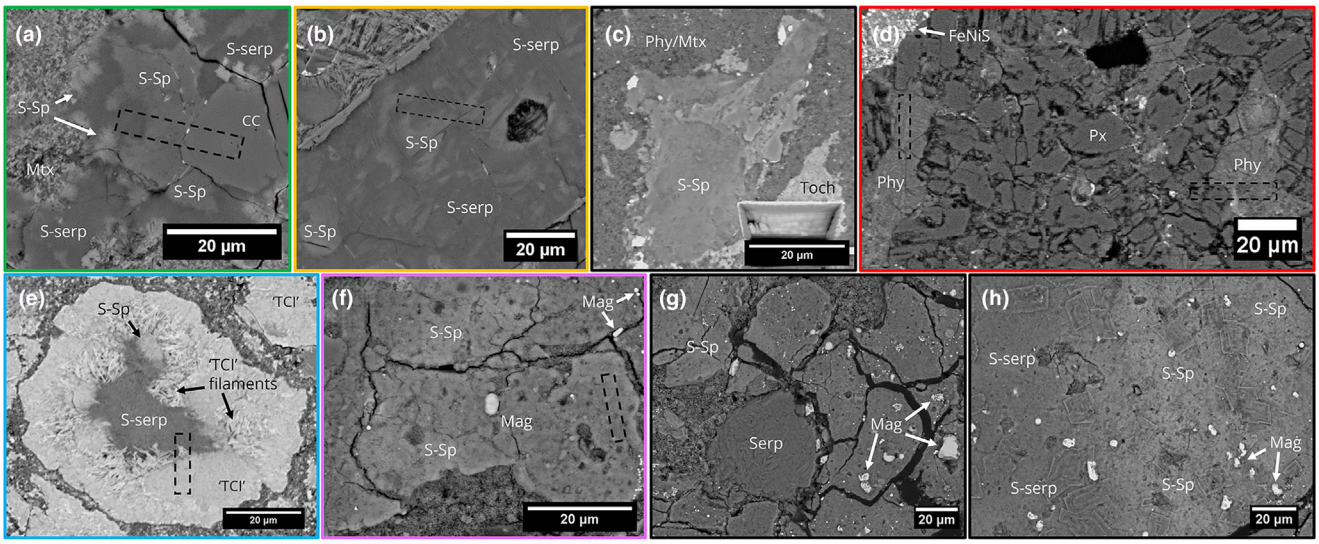

FIGURE 3. BSE images of representative textures and occurrences of S-bearing serpentines in CM and CI CCs. (a–c) Winchcombe and (D–E) Aguas Zarcas, (f–g) Ivuna and (h) Orgueil. S-bearing serpentines were initially qualitatively identified using SEM-EDS. (e) Characteristic "TCI-like object" in Aguas Zarcas; these typically have a Mg-rich serpentine core surrounded by an Fe-S-rich phase, with acicular TCI filaments at the edges of the serpentine core. CC, $CaCO_3$; Mag, magnetite; Mtx, matrix material; Phy, phyllosilicate; Serp, serpentine; S-serp, S-bearing serpentine; S-Sp, S-rich serpentine; Toch, tochilinite. Colored borders correspond to the regions outlined in Figure 2 showing where TEM lift-outs were prepared; lift-out locations denoted by black dashed boxes.

There appears to be no correlation between the presence of sulfides and serpentine composition.

Type II TCIs (Suttle et al., 2021; references therein) are found in both Winchcombe and Aguas Zarcas, but are more dominant in Aguas Zarcas. In Winchcombe, they occur mostly in lithology B only (Suttle et al., 2024). TCI-like objects are readily distinguished from the matrix, occurring as isolated or clustered "clumps," with a light gray appearance in BSE images and well-defined boundaries (Figure 3e, TCI-like object). Most TCI-like objects defined here are zoned, with Fe-sulfide-like rims and Mg phyllosilicate (serpentine) cores and have fibrous textures. The inner rims have acicular growths radiating into the serpentine cores. In some instances, the cores of these objects are filled by calcite rather than phyllosilicate.

There is some correlation between sites of S-rich and S-bearing serpentine and TCI-like objects; particularly in Aguas Zarcas all identified sites of S-bearing serpentine have been serpentines in the cores of these objects. S-rich serpentine was observed as a radial growth at the edge of a TCI rim in Aguas Zarcas (Figure 3e). However, in Winchcombe, with the exception of one site where S-rich serpentine was found associated with tochilinite (Figure 3c), there is little correlation between TCI-like objects and S-bearing or S-rich serpentines.

Similarly, there is little-to-no correlation between sulfides in Winchcombe and Aguas Zarcas and the occurrence of S-bearing or S-rich serpentines. Where sulfides have been partially altered to form phyllosilicates, these were not considered in our analyses of sulfur in serpentines due to their proximity to the primary sulfide and intermixing of the two phases.

(S)TEM Analyses

Based on initial characterization using SEM-BSE imaging and SEM-EDS, sites for FIB lift-outs were identified on Winchcombe, Aguas Zarcas, and Ivuna, as indicated by the black dashed boxes in Figure 3. High-angle annular dark-field (HAADF) and bright-field (BF) STEM images of some of these lamellae are shown in Figure 5a–e. All show the characteristic fibrous texture of serpentine, and a mix of fine- and coarse-grained material. Figure 5a of Winchcombe site B (see Figure 3b) shows acicular coarse-grained serpentine with large fibers intergrown with more fine-grained material, where the lighter gray contrast correlates with sulfur abundance. Generally, in Winchcombe, the finer-grained serpentines have lower sulfur abundances (e.g., left-hand side of Figure 5a) compared to the larger serpentine "mats" such as the band of S-rich serpentine running through the center of Figure 5a.

BF-STEM images of Aguas Zarcas (Figure 5b,c; lamellae locations Figure 3d,e) also show similar textural differences in serpentine with correlations between grain size and sulfur abundance. A key difference is the larger, non-fibrous grains in the upper left of Figure 4b. This

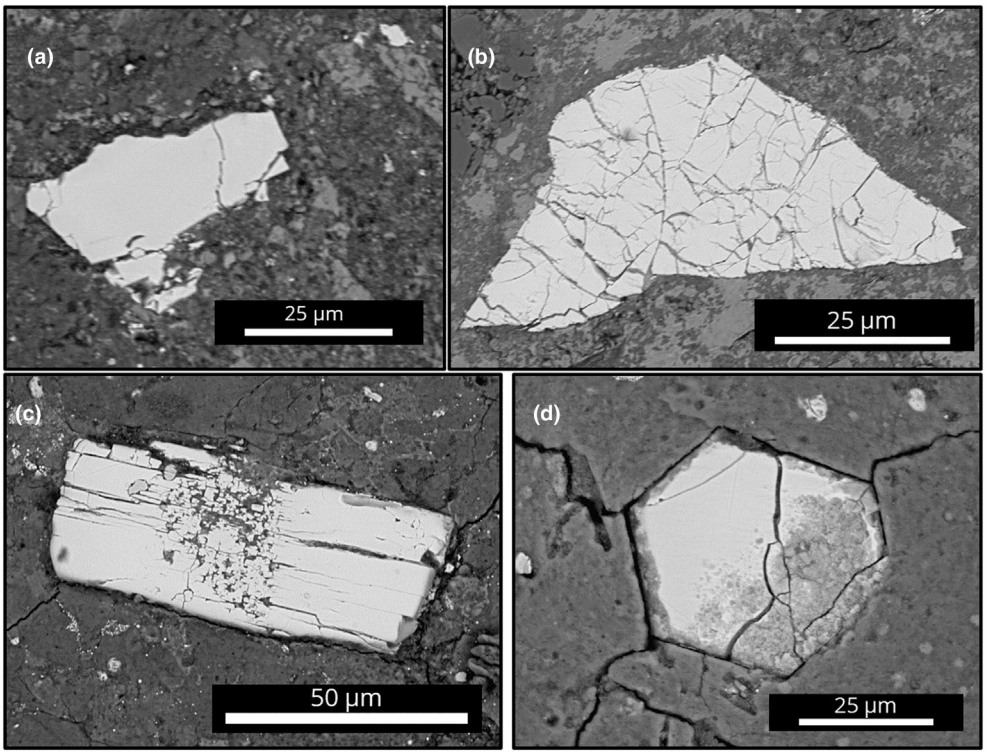

FIGURE 4. Representative sulfides present in the samples studied. (a) Winchcombe, Ni-rich sulfide, pentlandite, $(Ni, Fe)_9S_8$. (b) Aguas Zarcas, Ni-rich pentlandite. (c) Orgueil, lathe-shaped pyrrhotite, $Fe_{1-x}S$, with some alteration to phyllosilicate at its center. (d) Ivuna, typical hexagonally shaped pyrrhotite showing corrosion and alteration to an Fe-sulfate and phyllosilicate on the right-hand side. Phases characterized via SEM-EDS analyses.

phase has indeterminate mineralogy; it is unclear whether this phase is like other S-bearing serpentines in the CMs; however, it does not have the composition expected of tochilinite or cronstedtite. Unlike other phyllosilicates studied here, Figure 5c has a platy appearance, where crystalline S-bearing serpentine surrounds partially crystalline clusters with little-to-no sulfur content.

Similar textures to those of Winchcombe and Aguas Zarcas serpentines in Figure 5a,b are observed in CI and CI-like samples. Ivuna (Figure 5d) has intergrown fine- and coarse-grained material, but is largely dominated by finer-grained serpentine with no magnetites or sulfides present in the lamellae studied. In Ryugu, (Figure 5e) there is a clear distinction between two serpentine morphologies: radial growths of larger, coarse-grained serpentine and fine-grained material with embedded magnetites and sulfides. Unlike in the other samples, there appears to be no correlation between S-bearing, S-rich serpentines and S-poor serpentine morphologies, as almost all serpentine analyzed in the Ryugu lamellae are S-poor.

Analysis of the S-bearing serpentines at the nanometer scale allowed us to check for any potential association with sulfides, and the possibility of sub-micrometer sulfides being embedded in the phyllosilicate material which was not resolved using SEM. In the BF-STEM images of Winchcombe, there is no association of S-rich and S-bearing serpentine with sulfides and there are no micro- to nanosized grains of sulfide present (Figures 5a and 7). In the lamellae taken from the TCI-like object in Aguas Zarcas (Figure 5e), there are some micrometer-sized sulfides present at the boundary between the fine-grained serpentine core and the outer Fe, S-rich rim. In HRTEM imaging, no nanometer-sized sulfides are seen within the serpentines. In Ivuna, there are no sulfides observed at the sub-micrometer level; however, texturally the serpentines are more acicular in nature and generally more Fe-rich, as well as S-rich or S-bearing. It is possible that some of the fibers in the lamella are phases such as ferrihydroxide, intermixed with the serpentine. In Ryugu, we observe some difference in the association of serpentine and sulfide distribution. Almost all serpentine analyzed in the Ryugu lamellae are S-poor (Table S3), and there is an increase in the number of sub-micrometer (<1 µm) sulfides relative to other carbonaceous samples. Several pyrrhotite-like sulfides are seen adjacent to a coarse-grained S-poor serpentine in Figure 5e, and a cluster of sub-micrometer sulfides is also seen with the fine-grained phyllosilicate, which is again S-poor. Overall, there appears to be an

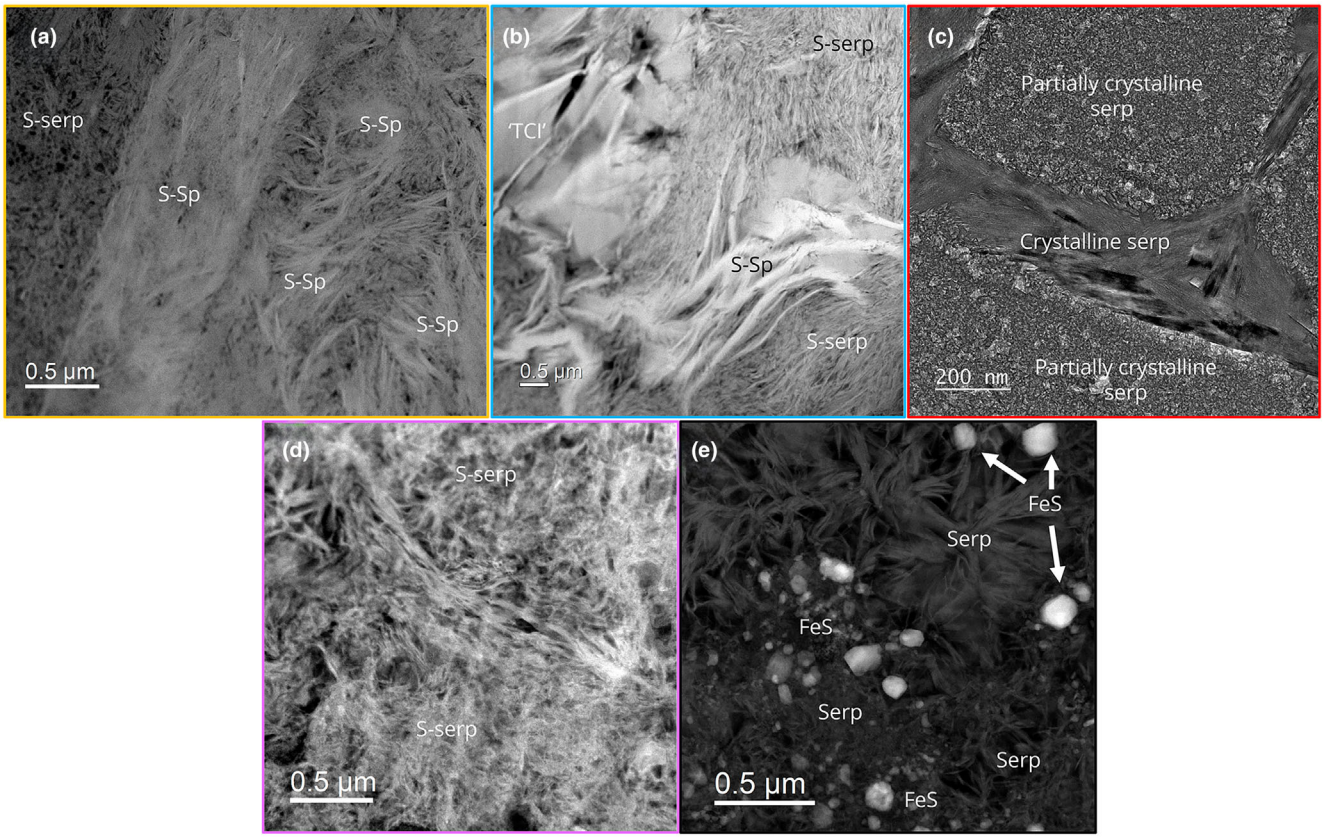

FIGURE 5. Representative sub-micrometer textures of serpentines in the CM and CI chondrites. Colored borders correspond to the colored borders of the regions shown in Figure 3. Top row: (a) HAADF-STEM image of serpentine and S-bearing serpentine in Winchcombe showing coarse- and fine-grained matted fibrous texture. (b) HAADF-STEM image of fibrous S-bearing serpentine in Aguas Zarcas, with large coarse filaments and finer-grained mats. (c) BF-STEM image of "platy" serpentine structure in Aguas Zarcas, consisting of crystalline serpentine surrounding partially crystalline regions. Bottom row: (d) HAADF-STEM image of fibrous serpentines observed in Ivuna. (e) HAADF-STEM image of Ryugu showing large radial growths of coarse-grained serpentine with smaller, fine-grained serpentine, and micro- and nanoscale magnetite and sulfide grains. S-serp = S-bearing serpentine, S-Sp = S-rich serpentine, Serp = serpentine.

anti-correlation between the abundance of sulfides and the abundance of sulfur within serpentine in the CMs.

TEM Lattice Spacings

Lattice spacing measurements were taken across S-poor, S-bearing and S-rich serpentine sites on TEM sections from Winchcombe, Aguas Zarcas, Ivuna and Ryugu (e.g., Figure 6). The d_{001}-spacings were found in the range 0.64–0.70 nm across all sites, where the average d_{001}-spacing for both the CMs and the CIs was equal to 0.68 ± 0.02 nm, within error of the expected 0.70 nm spacing of serpentine (Hicks et al., 2014; Zega et al., 2006). Figure 6 shows the lattice structure observed when looking along the (1 0 0) or (0 1 0) planes, that is, with the electron beam oriented perpendicular to the (0 0 1) basal planes, with the structure visible as repeating two-layer units. The two layers are the pairing of an octahedral (O) cation layer with a tetrahedral (T) layer, making a 1:1 layered T-O phyllosilicate, characteristic of serpentine (Hicks et al., 2014; Zega et al., 2006). There was a near absence of smectite-like lattice spacings ~1.0 nm (Deer et al., 1992; Hicks et al., 2014) in the areas analyzed.

Winchcombe site B was selected, due to the clear distinction between S-bearing and S-rich serpentine regions, for more detailed analyses into whether sulfur abundance has any effect on the lattice spacings observed (Figure 6). Some measurements in the S-rich regions appear to indicate a reduced d_{001}-spacing of 0.64 ± 0.02 nm. Initial evaluation of this relationship in Winchcombe produced a correlation coefficient, $R = -0.963$, indicative of an anti-correlation between sulfur abundance and lattice spacing; as sulfur content increases, the d_{001}-spacing decreases (see Figure S2). However, further work is needed, as initial comparisons with the other samples do not provide further clarity on this finding.

A tochilinite lamella from Winchcombe (Figure 3c) was used for measurements of tochilinite lattice spacings,

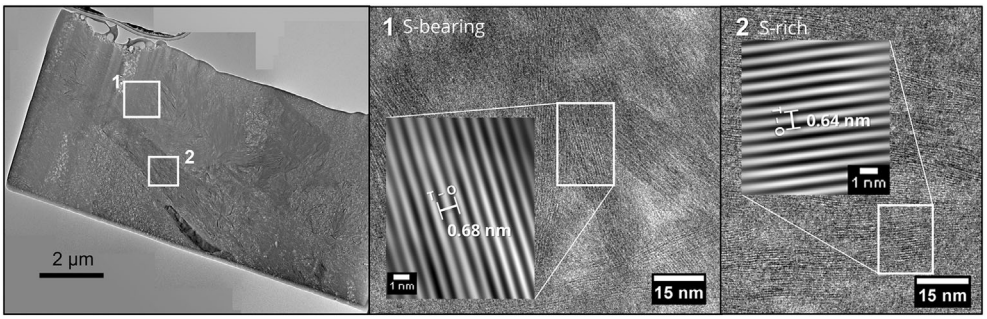

FIGURE 6. Insets show inverse Fourier-filtered images of S-bearing and S-rich serpentines, from Winchcombe Site B (Figure 3a). Basal lattice spacings were found in the range 0.64–0.70 nm for all serpentines in Winchcombe, with an average of 0.68 ± 0.02 nm, within error of the expected value for serpentine (Hicks et al., 2014; Zega et al., 2006). Spacings were determined via HRTEM imaging and measuring an average of five sites per image, by selecting crystalline regions, applying a fast Fourier transform (FFT) and taking the average over as many peaks as possible in the resulting plot. The top left overview image is a composite of several images, hence the appearance of artifacts in the form of contrast steps towards the top right.

which were found to be $\sim 0.54 \pm 0.02$ nm, as expected for the d_{002}-spacing of tochilinite (Mackinnon & Zolensky, 1984; Organova et al., 1973; Pekov et al., 2013; Vacher et al., 2019). By comparing the tochilinite second-order reflections identified here, and the basal lattice spacings given in the literature (0.54 and 1.1 nm, respectively) (Mackinnon & Zolensky, 1984; Vacher et al., 2019) to those of the S-bearing serpentine, we further confirm we are observing a serpentine phase and not tochilinite.

Furthermore, the serpentine d_{001}-spacings identified do not correlate with the basal spacings of TCIs, which constitute interstratified layers of tochilinite and serpentine/Fe-rich serpentine (cronstedtite), and these TCIs are found to have spacings in the range of 1.70–1.84 nm (Lauretta et al., 2000; Peng et al., 2007; Peng & Jing, 2014).

Composition of S-bearing Serpentine

Compositional characterization of regions of interest (ROI) has been carried out using SEM-EDS, while STEM-EDS was used for higher spatial resolution EDS characterization. High-spatial resolution EDS is crucial for local, nanoscale compositions in order to avoid mixing of signals from different phases, which is particularly important in this work, for example to avoid nanosized sulfides near the serpentines. In addition to Ivuna and Orgueil, due to its CI-like composition and similarities to the CI chondrites (Nakamura et al., 2022; Yada et al., 2022) Ryugu has been included in these analyses as a pristine comparison, as it is known that both Ivuna and Orgueil (in particular) have experienced some degree of terrestrial weathering (Gounelle & Zolensky, 2001, 2014; King et al., 2020).

S-bearing serpentine is observed in both the CMs and the CIs. We have defined that where sulfur content is ≥ 10.0 wt% SO_3 (equiv.), this is sulfur-rich ("S-rich") serpentine. Anything below this amount is designated as S-bearing. Where sulfur is not detected, this is simply referred to as serpentine. Results from both SEM-EDS and STEM-EDS are plotted on a (Si + Al) – Mg – Fe ternary, shown in Figure 8, with full compositional information and site occupancies of the different phases shown in Table 1 (STEM-EDS analyses, including Ryugu, are shown in Table S3). In order to determine a suitable mineral formula for sulfur-bearing serpentine, sulfur abundances are recorded as HS^- and $(SO_4)^{2-}$ equivalent, based on the sulfur species identified via S-K edge XANES in S-K and Fe-K XANES Analyses Section. The raw compositional data were recorded as SO_3 wt% equivalent, and then converted to the relevant HS^- and $(SO_4)^{2-}$ abundances using the $S^{6+}/\Sigma S_{total}$ ratios determined from the S-K edge XANES (see Supporting Information for further detail).

In the two CM samples studied here, S-rich serpentine is more prevalent in Winchcombe than in Aguas Zarcas. Although sulfur has been detected in serpentine in Aguas Zarcas it is mostly S-bearing rather than S-rich; however, there are a few instances of S-rich serpentine, for example at the rims of TCI-like material surrounding serpentine formations (see Textures and Occurrence of S-bearing Serpentine Section and Figure 3e). This is further confirmed with STEM-EDS measurements. For the CIs, SEM-EDS (Orgueil) and STEM-EDS (Ivuna) analyses were carried out on the brighter regions seen in BSE images (Figure 3f–h) corresponding to greater sulfur (and Fe) concentrations. The exception is Ryugu as there are no SEM-BSE images prior to TEM lift-out; however, several points with increased sulfur abundance in the phyllosilicates were still detected.

As discussed in Textures and Occurrence of S-bearing Serpentine Section, visually brighter BSE regions of serpentine correspond to increased sulfur concentrations.

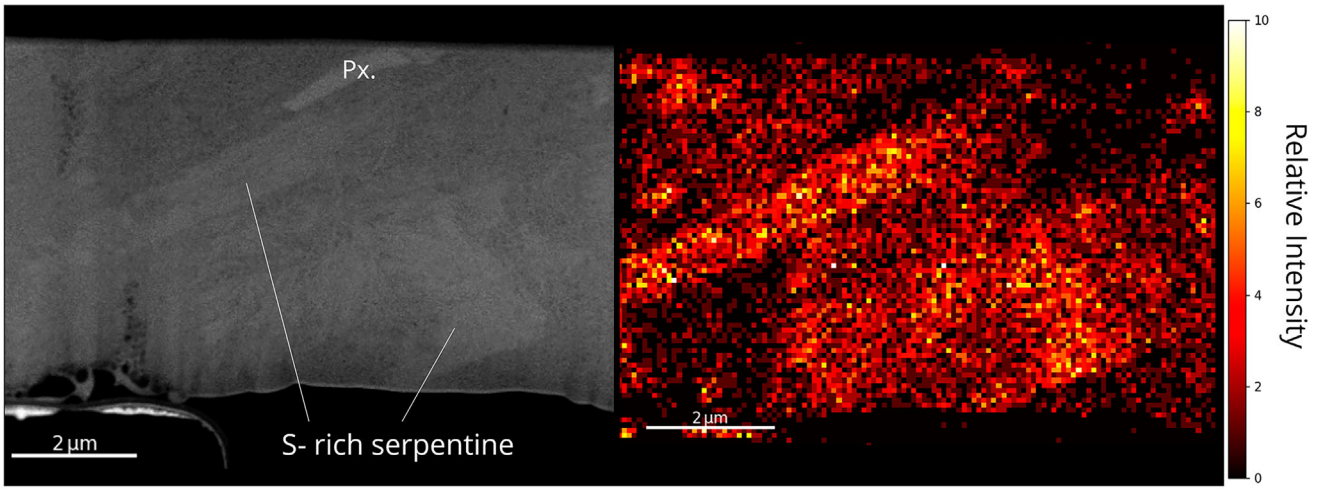

FIGURE 7. Left: HAADF image of Winchcombe site B lamella, extracted from the site shown in Figure 3b, where the brighter gray regions correspond to S-rich serpentine. Darker grays correspond to regions of S-bearing serpentine. Right: STEM-EDS map showing the intensity and distribution of sulfur across the lamella, where sites of increased intensity can be seen to correlate with the S-rich serpentine on the left HAADF image. The same site was further selected for analysis using 4D STEM and correlative EDS due to the clear distinction between the two phases (Figure 11). Px, pyroxene.

This was also seen at the sub-micrometer scale using EDS mapping, as shown in the sulfur map of Winchcombe site B in Figure 7. The relative intensity of the S-rich serpentine is greater than that of the surrounding Mg phyllosilicate, owing to both sulfur being a higher Z element than Mg (S, $Z = 16$; Mg, $Z = 12$) and greater sulfur abundance in these regions. These areas of greatest intensity also correlate with the brighter, S-rich serpentine in the left-hand dark-field image of Figure 7.

The greater sulfur content relating to higher intensity (Figure 7) is evidenced by STEM-EDS measurements in the same areas; the most intense regions have sulfur content of ~9.7 wt% SO_3 equivalent while the rest have ~3.2 wt% SO_3, corresponding to our definitions of S-rich and S-bearing serpentines. While whole sample EDS maps were not taken of the Aguas Zarcas and Ivuna lamella, sulfur maps were produced at a local scale of the ROI where EDS data were collected, and also showed that in the fibrous serpentines of these two samples sulfur is present across the ROIs, but not in the form of sulfide grains. Again, EDS on these ROIs in the lamella confirms a significant variation in the abundance of sulfur in the serpentine compositions.

The exceptions to these findings are Orgueil and Ryugu. While some S-bearing serpentine was identified in the Ryugu lamella studied, it was not as prevalent as in the other samples with only a small number of S-bearing serpentine grains found (representative compositions are shown in Table S3). In Orgueil, SEM-EDS results showed that all S-bearing serpentines in this sample are actually S-rich; that is, all the compositions have sulfur abundances ≥10.0 wt% SO_3. For Ryugu, consideration needs to be given in regard to the sampling site(s) of Hayabusa2, and for Orgueil the effects of terrestrial weathering. These are discussed further in PCPs, TCIs and Sulfur-bearing serpentine in the CM Chondrites Section.

In the phyllosilicate ternary plot (Figure 8), it can be seen that most values for both the CMs and CIs lie close to the stoichiometric solid-solution line of serpentine and do not lie within the typical plotting area of TCIs in CM chondrites (Suttle et al., 2021), nor on the tochilinite-cronstedtite mixing line (Palmer & Lauretta, 2011). There is some spread on either side of the serpentine solid-solution line, and this suggests that there is a range of compositions for these serpentine-like phyllosilicates in meteoritic materials and which cannot be tied to one ideal stoichiometry model. For Ryugu, this compositional range has been presented in several other studies of Ryugu phyllosilicates (Ito et al., 2022; Nakamura et al., 2022, 2023; Yamaguchi et al., 2023). A more recent study by Aléon-Toppani et al. (2024) suggests there is compositional range observed in Ryugu phyllosilicates due to differences between the coarse- and fine-grained textures (30–100 nm width and <10–30 nm width, respectively), where coarse-grained phyllosilicates have compositions that fall between saponite and serpentine, and fine-grained phyllosilicates are more saponite-like. Due to the scatter of serpentine compositional values seen in Figure 8, showing that serpentine stoichiometry can vary across sample types, a further important question is to determine the proportion of these phyllosilicates that are saponite, based on lattice spacing information.

Some tochilinite was also found in Winchcombe via SEM-EDS and a TEM lift-out made from the region, for

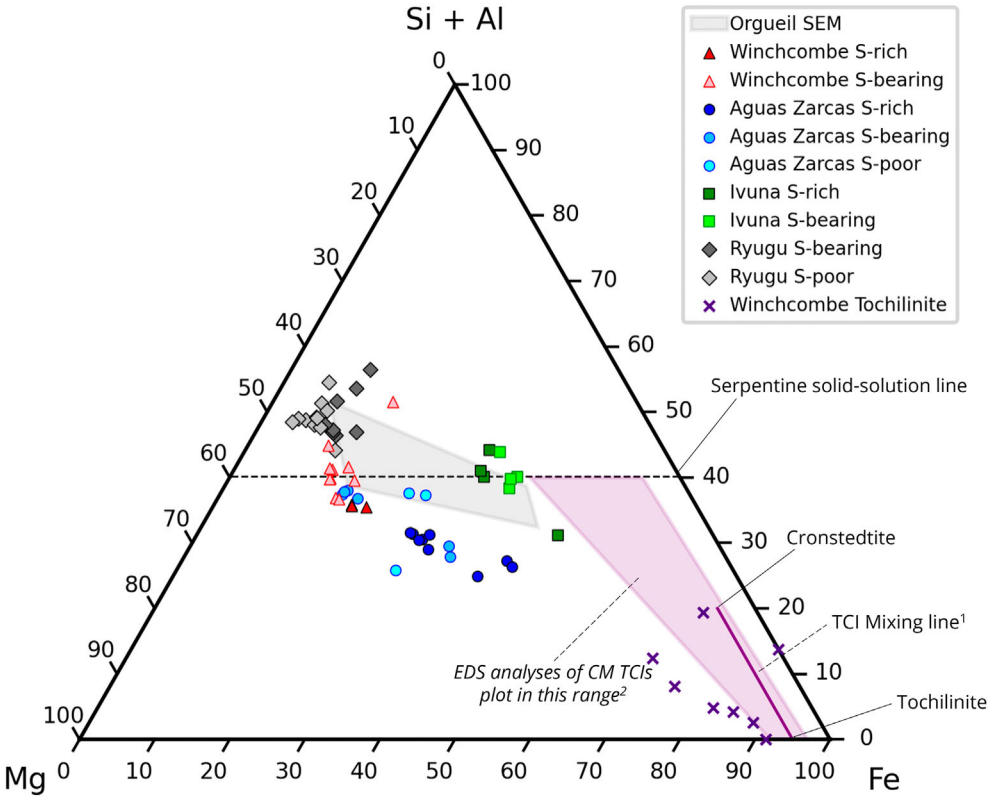

FIGURE 8. STEM-EDS (Orgueil only) and TEM-EDS plotted on an (Si + Al)–Mg–Fe_{total} ternary in atomic %. The S-bearing serpentine values largely cluster around the serpentine solid-solution line. No points lie within the expected regions for TCIs and nor do they plot close to stoichiometric tochilinite or on the tochilinite–cronstedtite tie line. Representative SEM-EDS compositional values are shown in Table 1, and representative STEM-EDS compositions are shown in Table S3. Serpentine values from Deer et al. (1992). Dark purple line = [1]Palmer and Lauretta (2011). Purple shaded region = [2]Suttle et al. (2021).

comparison to the S-bearing serpentine analyses. Tochilinite varies in composition compared to serpentine as it has much higher S and Fe content, ~30–40 wt% SO_3 equivalent and ~40–50 wt% FeO equivalent, and much lower Si content, $\sim \leq 10$ wt% SiO_2 (King et al., 2022; Mackinnon & Zolensky, 1984; Vacher et al., 2019) (see also Table S3 for tochilinite analyses from this study). Therefore, based on the compositions observed in S-bearing serpentines, the lattice spacings and comparing to tochilinite, we can confirm we do not observe tochilinite or tochilinite–serpentine mixtures in the ROI analyses plotted in Figure 8 and shown Table 1.

S-K and Fe-K XANES Analyses

To constrain the valence state of sulfur found in S-bearing serpentines, a set of standard sulfur compounds covering the range of sulfur valences was analyzed as reference materials. Figure 9 shows all S-K XANES spectra from the analyzed standards: sulfides (S^{2-} and/or S^{-}), sulfur (S^0) and sulfates (S^{6+}). Each of the spectra is characterized by an intense edge peak, followed by a broad shoulder or further oscillations, relating to the probability of absorption of the incident photon due to the local atomic structure around the emitting atom. Table 2 shows the measured edge position values of the standards used in this experiment, along with two standards taken from literature.

The edge position of the Fe-sulfides (chalcopyrite, pyrite) is between ~2470 and 2472 eV. Sphalerite differs slightly and has an edge position at ~2474 eV, and the usual prominent edge peak of ~2470–2472 eV for sulfides is absent from the sphalerite spectrum. It has been noted in previous studies (Debret et al., 2017; Fleet, 2005; Wilke et al., 2011) that when Zn is incorporated (as in sphalerite) the usual "sulfide peak" disappears and there are considerable oscillations preceding the edge position, as seen in Figure 9. The sulfates (anhydrite, $MgSO_4$, barite, gypsum) have the highest energy edge positions and display a strong peak at ~2482 eV (Figure 9). The various oscillations proceeding this intense peak vary in position and intensity for the different sulfates depending on the structural bonding environment around the sulfur.

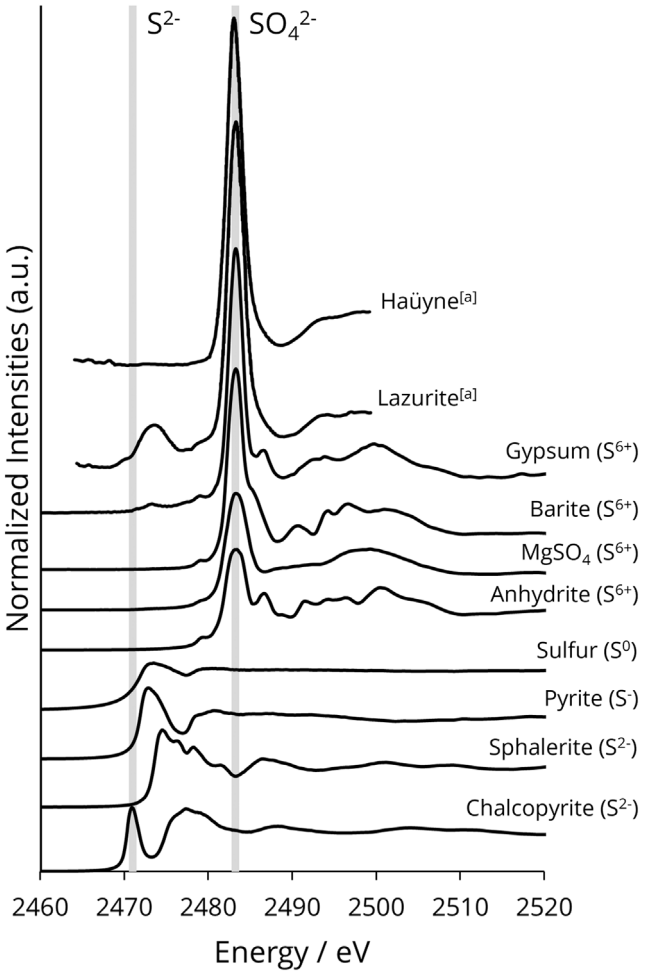

FIGURE 9. Plot of normalized S-K edge XANES intensities against energy (eV) for the sulfur-bearing compounds used as standards in this experiment. Compounds are ordered from those with reduced S^{2-} to those with oxidized S^{6+}. The absorption edge energies for S^{2-} and S^{6+} are marked in gray. [a] S-K XANES data from Fleet (2005).

The S-K XANES spectra of the serpentines in the CM and CI samples are shown in Figure 10. The XANES spectra of known tochilinite and Fe-sulfide phases have been included to demonstrate the difference between the sulfur-bearing serpentine phases and other S-bearing minerals in the CMs and the CIs. The peak energies and shapes of the sulfur-bearing serpentine phases were compared to the reference spectra collected. Table 3 shows the energy values of the main absorption edges in the spectra, along with other notable features.

The spectra displayed in Figure 10 of the CMs and the CIs are summed spectra of both the S-bearing and S-rich serpentines, and the low sulfur serpentines. Representative, individual spectra from Winchcombe are also plotted in Figure 10, and show that even in singular spectra, the characteristic peaks for S^{2-} and S^{6+} are still

TABLE 2. Main XAS features of sulfur standards as measured in the S-K edge XANES experiment.

Standard	Formula	Edge position (eV)
Chalcopyrite	$CuFeS_2$	2470.2
Pyrite	FeS_2	2471.8
Native sulfur	S	2472.0
Sphalerite	(Zn, Fe)S	2473.5
Anhydrite	$CaSO_4$	2481.8
Magnesium sulfate	$MgSO_4$	2482.0
Barite	$BaSO_4$	2482.2
Gypsum	$CaSO_4{\cdot}2H_2O$	2482.2
Haüyne[a]	$Na_6Ca_2(Al_6Si_6O_{24})(SO_4)_2$	2481.7
Lazurite[a]	$Na_7Ca(Al_6Si_6O_{24})(SO_4)(S_3) \cdot H_2O$	2472.2, 2481.9

Note: Mineral formula for haüyne and lazurite taken from Hassan and Grundy (1991) and Sapozhnikov et al. (2022), respectively.
[a]Literature values for haüyne and lazurite from Fleet (2005). Other literature values from ESRF (2018).

clear. From the annotated sites shown in Figure 10, it can be noted that even in sites designated S-bearing (rather than S-rich), we are still able to retrieve S-K edge XANES individual spectra from these regions. Comparing the measured edge positions to those of the standards, we found that in the CMs the sulfur has valencies S^{2-} and S^{6+}, and in the CIs the sulfur has valences S^{-} and S^{6+}. In some spectra, notably those with larger S^{6+} intensities, a small pre-edge feature is observed at ~2478.5 eV. This feature is likely due to the reduction of S^{6+} to S^{4+} by the X-ray beam (Lerner et al., 2021; Wilke et al., 2008), and with varying broadness due to the presence of a second, wide absorption feature seen in sulfides (see Figure 9). In the tochilinite spectrum (Figure 10), an additional peak centered around 2473 eV is observed and can be attributed to the H-S bond in tochilinite (Prange et al., 2002).

The abundances of the two endmember species identified can be estimated using S-K edge XANES spectra as abundance correlates with peak amplitude (Anzures et al., 2020; Fleet 2005). To estimate the relative abundances of S^{2-} and S^{6+} in the samples, LCF of the standards to the samples was performed (Ravel & Newville, 2005). Combining LCF and comparing edge positions and appearance of the spectra to the standards, we have identified that the dominant sulfur oxidation state in the CM chondrites is S^{2-}, with some oxidized sulfur, that is, S^{6+}. In the CI chondrites, we observed the opposite; in Ivuna, the dominant phase is purely oxidized sulfur, S^{6+}, and in Orgueil it is both oxidized and reduced sulfur; however, the valency of the reduced sulfur is S^{-} rather than S^{2-}. Again, for Orgueil in particular we note that the valency of sulfur may be affected by terrestrial weathering.

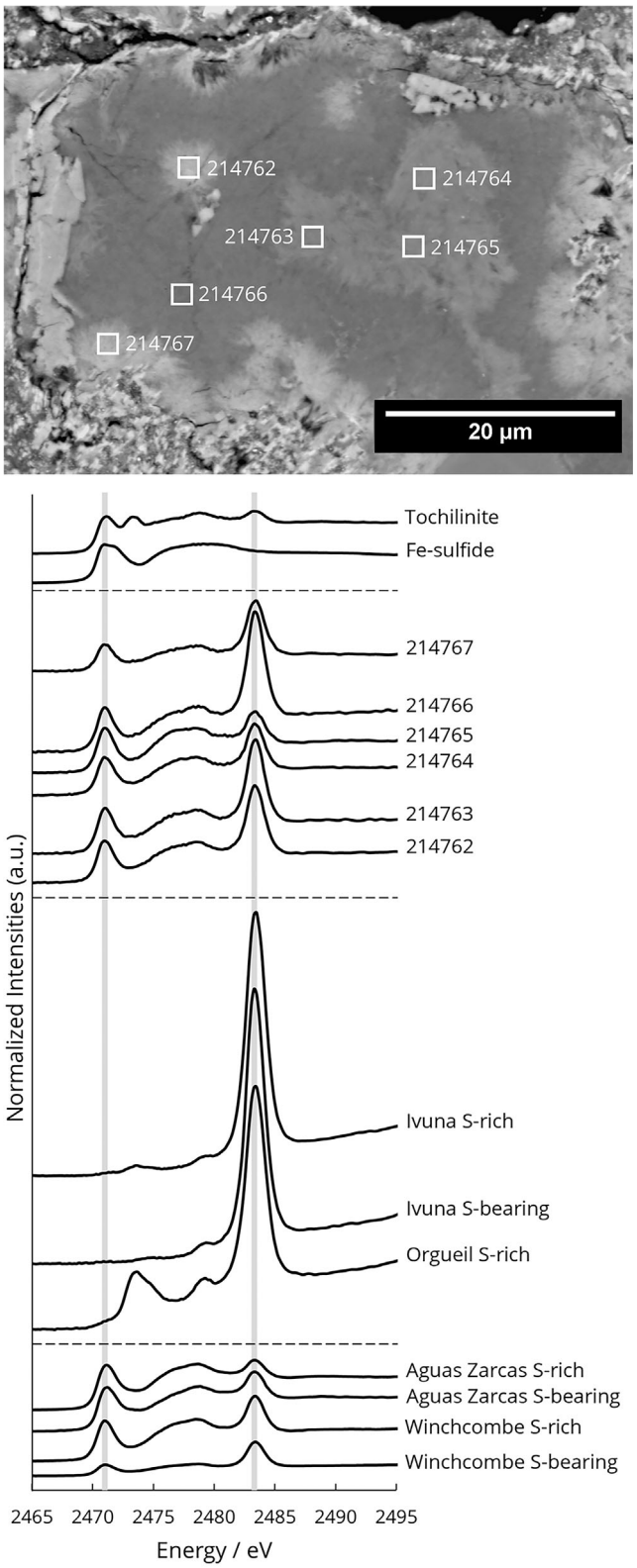

FIGURE 10. Plot of representative summed S-K XANES spectra of the CM and CI chondrites, including individual spectra from sulfur-serpentine sites in Winchcombe. The gray lines correspond to the absorption edge energies of S^{2-} and S^{6+}. Spectra were summed for the different samples to show an average spectrum for that particular phase; that is, multiple measurements were taken of the same phase(s) from different sites in each sample. Individual spectra are shown for the annotated sites in Winchcombe, showing that the characteristic peaks are still easily retrievable from individual spectra. Representative tochilinite and Fe-sulfide spectra are shown for comparison.

Results from Fe-K edge XANES analyses found that the serpentines have $Fe^{3+}/\Sigma Fe$ ratios equal to 0.57 ± 0.04 so they have higher ferric content, while the sulfur-bearing serpentines have ratios equal to 0.48 ± 0.04 and are, therefore, slightly more ferrous. Estimations for both serpentine and S-bearing serpentine $Fe^{3+}/\Sigma Fe$ ratios averaged $\sim 0.55 \pm 0.04$, despite their differing compositions (Table 1 and Tables S1 and S3), but roughly there is a 50:50 split across the two Fe species present in sulfur-bearing serpentines, which is only a minor difference compared to S-poor serpentine. Further details are reported in Supporting Information S1.

4D STEM and Correlative EDS

The BF-STEM images in Figure 11 show the regions in the Winchcombe site B lamella which were examined using nanobeam 4D STEM (convergence angle ~1 mrad) and correlative EDS, along with a higher magnification image of the area discussed in further detail here, which shows the typical heterogenous mix of fine- and coarse-grained phyllosilicates; both S-rich serpentine (the darker triangle-shaped area) and S-bearing serpentine surrounding it. The identification of these regions as serpentine and their sulfur content was confirmed via both structural and compositional analyses prior to 4D STEM and correlative EDS data collection (see previous TEM Lattice Spacings and Composition of S-bearing Serpentine). Nanobeam 4D STEM data was first reduced via radial profile analysis (see Supporting Information S3 for details), and NMF was used to segment the data into a linear combination of loading vectors, representing strong Bragg reflections. Here, the data was segmented into 20 loading vectors which best represented the original dataset (Ryu et al., 2021; Uesugi et al., 2021). The loading vectors were categorized into three groups; those that represent serpentine, S-bearing serpentine and others (the latter includes contributions from noise, background signal, amorphous and/or complex mixes, and an unidentified/under-reported phase). Out of the 20 loading vectors extracted, only loading vectors 5 and 19 are interpreted below as these best represent the two phyllosilicate phases being studied here, and both loading vectors show compositional and structural (d-spacing) differences based on the two sulfur-bearing serpentine

TABLE 3. Absorption edge energies identified for the different features of serpentines in the CM and CI chondrites.

	Phase	Main absorption edge position (eV)	Other peaks (eV)
Sample name			
Winchcombe	Tochilinite	2470.3	2473.3, 2478.9, 2482.6
Ivuna	Fe-sulfide	2470.2	
Winchcombe	S-rich serpentine	2470.2	2478.5, 2482.2
	S-bearing serpentine	2470.3	2478.7, 2482.3
Aguas Zarcas	S-rich serpentine	2470.3	2478.7, 2482.6
	S-bearing serpentine	2470.2	2478.9, 2482.6
Ivuna	S-rich serpentine	2482.5	2472.6, 2478.3
	S-bearing serpentine	2482.5	2473.3, 2478.3
Orgueil	S-rich serpentine	2482.3	2472.6, 2479.3
Site number			
214762	S-rich serpentine	2470.3	2478.5, 2482.2
214763	S-bearing serpentine	2470.3	2478.5, 2482.3
214764	S-bearing serpentine	2470.3	2478.5, 2481.9
214765	S-bearing serpentine	2470.3	2478.3, 2482.6
214766	S-bearing serpentine	2470.3	2478.7, 2482.4
214767	S-rich serpentine	2470.3	2478.5, 2482.3

Note: The main energy of the absorption edge peaks are shown, along with any other notable peaks in both the summed and individual spectra. Absorption edge energies were measured as the energy of the normalized spectra at an intensity of 0.5 (a.u), that is, at FWHM. The error on all measurements is ±0.2 eV.

phases. The remaining outputs for the other loading vectors are shown in section S6 of the Supporting Information.

Figure 11 (top right panel) shows a virtual bright-field image (vBF) of the 4D STEM and EDS dataset. Loading vector maps for two of the loading vectors (LV) chosen here are shown in Figure 11, overlaid on the vBF image, where blue corresponds to LV 5 and purple to LV 19. These are threshold maps, showing the highest coefficients which contribute to each loading vector. These maps show which phases are present that are producing the corresponding diffraction patterns in the dataset, but it should be noted that not all S-bearing serpentine (and other phases) are represented by one loading vector; it is the case that one phase may be represented by several loading vectors. Two are shown here for simplicity. The averaged radial variance profile (RVP) of the pixels with the highest coefficients (≥90% threshold) for the same two loading vectors is shown in the bottom two panels of Figure 11. That is, the averaged RVPs originate from the data produced when using a threshold to generate the high-coefficient maps. The normalized coefficient maps, averaged RVPs and the summed original loading vector RVPs are presented in the Supporting Information for all 20 LVs.

In agreement with literature values (Brindley & Brown, 1984; Hicks et al., 2014; Mellini, 1982; Mellini et al., 2010; Viennet et al., 2023) the peaks located at 7.02, 3.66, and 2.54–2.57 Å in Figure 11 correspond to the 001, 002 and 111 lattice planes of serpentine, respectively. The SD of all 001 reflections identified across all loading vectors (total number of loading vectors was 20) is $\sigma \sim 0.22$ Å. The additional peak at 4.57 Å in the bottom right panel of Figure 11 corresponds to the 100 plane, and based on our findings with conventional HRTEM and STEM-EDS in this work, the peak located at ~6.39 Å could be attributed to S-bearing serpentine. While this feature only appears in one loading vector, it is still a genuine feature as the high-coefficient map area is unique, and does not have the random scattering associated with noise. The peak can also be seen in the summed RVP for this area.

To further constrain the 4D STEM results, correlative EDS data were collected simultaneously with the 4D STEM data. Qualitative analysis of the EDS spectra found that both LVs represented S-bearing serpentine, with LV 19 being more S-rich than LV 5 (around double the SO_3 equivalent abundance). Both LVs also displayed a phyllosilicate-like composition. Initial quantitative EDS results are shown in Section S5 (Table S4). Full quantification to determine relative abundances is ongoing and will form future work in the application of this new technique to more planetary materials. Combining the EDS spectra and the structural information from the 4D STEM, it demonstrates that 4D STEM and correlative EDS show the association of sulfur with serpentine phases in CC samples.

DISCUSSION

PCPs, TCIs and Sulfur-bearing Serpentine in the CM Chondrites

Fe, S-rich phyllosilicate-like phases were first called PCPs by Fuchs et al., 1973. Since then, many studies of

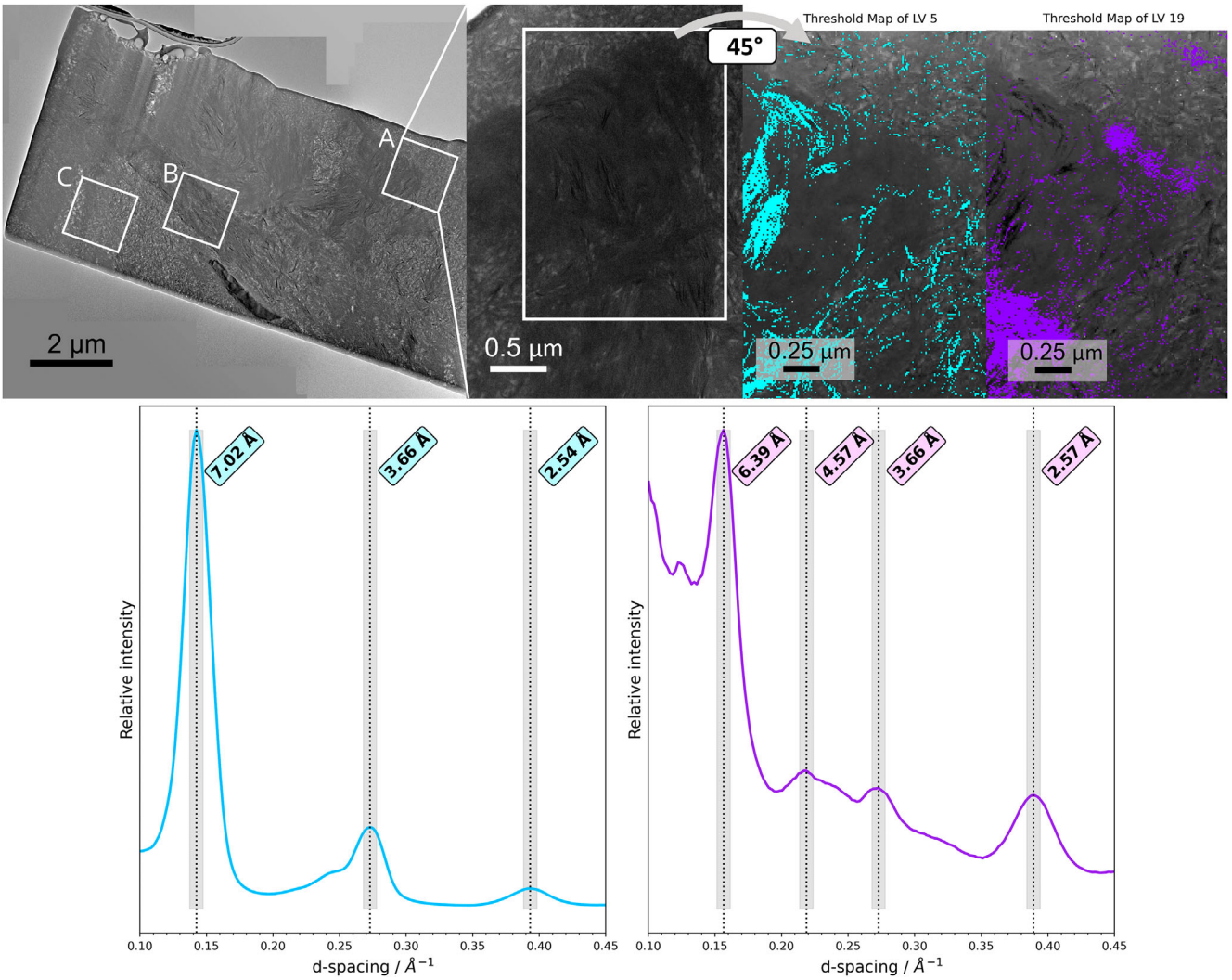

FIGURE 11. Top: The left and center panels show BF-STEM images of the Winchcombe lamella from site B. The boxes labeled A–C show the regions where both 4D STEM and correlative EDS data were collected. Region A (center panel) shows the heterogeneous mix of fine- and coarse-grained phyllosilicates, typical of this sample type. The right-hand panel shows the reconstructed virtual bright-field (vBF) STEM image of the same region A (rotated 45°) with the high-coefficient threshold maps overlayed. The threshold maps show the pixels with the highest coefficients (top 10%) for each loading vector. The threshold data are used to produce the averaged radial profile plots; thus, these plots correspond to the 10% highest coefficients for each loading vector. Blue corresponds to loading vector 5, and purple to loading vector 19. Bottom: Two plots showing the 1D averaged radial variance for each loading vector and the corresponding lattice spacings, following the same color scheme as the maps. The dashed lines with gray shading highlight the peaks with attributed spacings. Though sulfur is found throughout this region, the phase represented by loading vector 19 is more sulfur-rich (nearly double) than the phase represented by loading vector 5 (Table S4). The peaks located at 7.02, 4.57, 3.66 and 2.54–2.57 Å correspond to the 001, 100, 002 and 111 lattice planes of serpentine, respectively (Brindley & Brown, 1984; Hicks et al., 2014; Mellini, 1982; Mellini et al., 2010; Viennet et al., 2023). Additionally, based on HRTEM measurements, the peak located at 6.39 Å can be attributed to the first-order reflection of S-bearing serpentine. The top left overview image is a composite of several images; hence the appearance of artifacts in the form of contrast steps towards the top right.

the CM and CI chondrites have identified these PCPs as clumps of tochilinite and cronstedtite intergrowths, TCIs (e.g., Krämer Ruggiu et al., 2022; Pignatelli et al., 2016; Tomeoka & Buseck, 1985; Zolensky, 1984). In several works, these PCP/TCI phases have also been described as serpentine-tochilinite intergrowths (e.g., Mackinnon & Zolensky, 1984; Rubin et al., 2007; Zega & Buseck, 2003); however, the descriptions of PCP/TCIs have been retained for these Fe, S-rich phyllosilicate intergrowths due to limited mineralogical characterization via electron microscopy techniques and the fine-grained nature of these phases. TEM studies by Tomeoka and

Buseck (1985) were able to place further mineralogical constraints on these PCP/TCI compositions, identifying them as Fe, Ni, S, O-rich minerals intergrown with cronstedtite. Based on these previous analyses, in subsequent works bright clumps of Fe, S-rich phyllosilicate-like material identified using SEM-BSE imaging and SEM-EDS have been classified as PCPs or TCIs. However, without mineralogical and structural analyses of these alteration products at both the micro and nanoscale, detailed compositions and classifications of these phases are not possible. By combining different techniques such as high-resolution electron microscopy and X-ray synchrotron analyses, we can improve upon the characterization of these abundant phases in the CCs.

From herein, all serpentine with >1 wt% SO_3 abundance (i.e., S-bearing and S-rich) is referred to as sulfur-bearing serpentine. From our correlative, multi-technique characterization of sulfur-bearing serpentine-like phases across several CM and CI chondrites, we suggest that there is another mineral phase present that is an intermediate stage of the progressive alteration of CCs, alongside true TCIs, and that rather than "serpentine-tochilinite intergrowth" or PCPs and "TCI-like" materials (e.g., Kerraouch et al., 2021; Lentfort et al., 2021; Rubin et al., 2007), there is generally sulfur-bearing serpentine instead. Our EDS analyses at the micrometer and nanometer scales found that the composition of the sulfur-bearing serpentine phase is closer to that of stoichiometric serpentine than tochilinite and/or cronstedtite. Nanoscale structural analyses further confirmed the phase as serpentine, with characteristic ~0.70 nm serpentine spacings and not the ~1.1 or ~0.54 nm spacings of tochilinite, or the ~1.75 nm spacings of TCIs. In the S-K edge XANES spectra, the peak at ~2473 eV attributed to the H-S bonding of tochilinite is unique to this spectrum and is not observed in the spectra of the S-bearing serpentines, further confirming the phase is not tochilinite. Future work would include re-examining more TCI-like phases across CMs with detailed SEM analyses, and STEM analyses for high-resolution compositional and structural information.

Location of Sulfur in Serpentine

From S-K edge XANES analyses, the valences of sulfur in serpentine have been identified as reduced sulfur, S^{2-}/S^{-}, and oxidized sulfur, S^{6+}, with the dominant valency differing between the chondrite types studied here. In both lazurite and haüyne, AlO_4 and SiO_4 tetrahedra are corner-linked and form cubo-octahedral cages which are able to accommodate different cations and anions such as Ca^{+}, SO_4^{2-} and S^{2-} (Deer et al., 1992; Hassan & Grundy, 1991; Wang, 2021). Serpentine displays a structure of pseudo-hexagonal vacancies formed by rings of six SiO_4 tetrahedra, which can accommodate small ions in their center (Brearley et al., 2007; Wunder et al., 2010). When comparing sulfur-bearing serpentine XANES spectra to haüyne (Figure 9, Table 1), as in Debret et al. (2017), it is important to note that the low-energy side of the absorption peak is largely featureless, and any absorption peaks in this range would be indicative of sulfur present in a reduced state (Fleet 2005). Therefore, a better comparison for the S-K XANES spectra observed for sulfur-bearing serpentine is lazurite (Figure 9, Table 1). Thus, owing to the similarities between both spectra of lazurite and haüyne, and following on from the work of Debret et al. (2017) and the identification of S^{6+} species in terrestrial abyssal serpentines via S-K XANES, we suggest the location of S^{6+} as SO_4^{2-} ions, located in the hexagonal vacancies of the serpentine tetrahedral layers. Finally, as both the sulfur-bearing serpentine and lazurite spectra share similar absorption peaks, this further supports the suggestion of sulfur trapped as SO_4^{2-} or S^{2-} ions in the structural vacancies, charge balanced by the presence of Fe^{3+}cations in the octahedra.

An additional suggestion for the location of reduced sulfur is that it is incorporated into the serpentine via partial replacement of OH^{-} groups as either S^{2-} or HS^{-}. During their study of serpentine nanotubes in the Mighei CM2-chondrite, Zega et al. (2004) suggested the formation of a new type of sulfur-bearing serpentine, where the sulfur substitutes for oxygen in the OH^{-} species, similar to the occurrence of sulfur in the S-bearing mica anandite (Filut et al., 1985). Sulfur was found to occur homogenously across the Mighei serpentine nanotubes by Zega et al. (2004) implying that it is an integral element of the serpentine and its structure. Similarly, we have found that where sulfur-bearing serpentine has been identified, the sulfur is distributed uniformly across it (Figure 12).

Based on previous works of Hicks et al. (2014) on Fe-serpentine and Zega et al. (2004) on sulfur-bearing serpentine, and the formula for the S-bearing mica anandite (Brindley & Brown, 1984), we suggest this sulfur-bearing serpentine has an approximate stoichiometric formula of $(Mg, Fe^{2+}, Fe^{3+}, Al)_{2\text{-}3}(Si, Al)_2O_5(OH)_{5\text{-}6}(HS^{-})_{1\text{-}2}(SO_4)^{2-}{}_{0.1\text{-}0.7}$ (Table 1).

Replacement of OH^{-} is possible in naturally occurring S-bearing micas (e.g., Filut et al., 1985) and via synthetic means by sulfidation of clays (e.g. Wang et al., 2020). The replacement could also occur via ligand exchange of the OH^{-} group by adsorption of S^{2-} or HS^{-} at the serpentine surface, as seen in other phyllosilicates (e.g., Feuillie et al., 2013). Although the H-S peak observed in S-K XANES spectra of tochilinite is absent in the sulfur-bearing serpentine spectra, this does not necessarily prove there is no H-S bonding at all in sulfur-

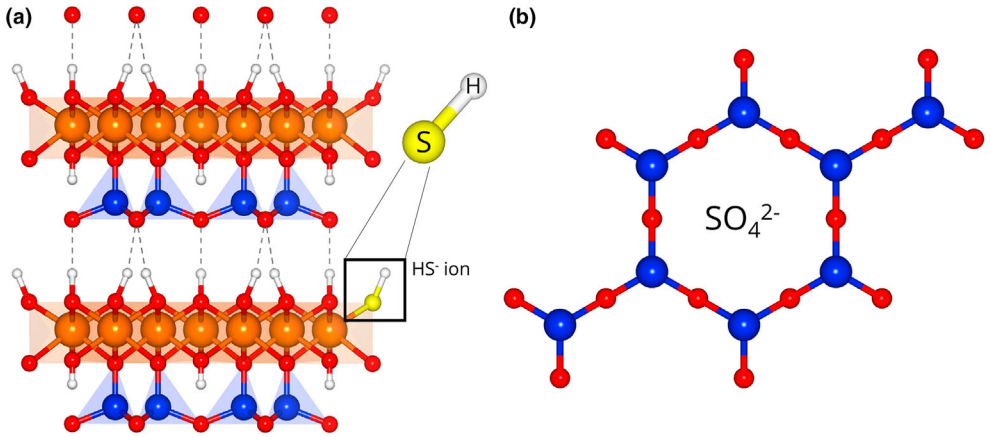

FIGURE 12. (a) Partial replacement of some OH^- ions by HS^- ions in the lattice of serpentine. (b) Possible location of sulfate ion in the hexagonal vacancies of the serpentine tetrahedral layer. The molecule is small enough to fit within the vacancy (size of hexagon > size of ion). This causes a charge imbalance but this may be mitigated by having ferric (Fe^{3+}) iron in the tetrahedra. Created using VESTA 3 (v 3.5.8) modeling software (Momma & Izumi, 2011)

bearing serpentine; it is plausible that as the concentrations are much lower in sulfur-bearing serpentine than in tochilinite (as seen in EDS comparisons, Composition of S-Bearing Serpentine Section) that this peak is unidentifiable in the S-K XANES spectra.

The reduced d_{001}-spacings of sulfur-bearing serpentine in some samples could be explained by the partial incorporation of SO_4^{2-} ions into the pseudo-hexagonal vacancies of the serpentine tetrahedra. As an analogy, in anandite (Ba, K)(Fe^{2+}, Mg)$_3$((Si, Al, Fe)$_4O_{10}$)(S, OH)$_2$, an S-bearing mica (Brindley & Brown, 1984), the interlayer Ba^{2+} ions are strongly attracted to the S^{2-} ions, shifting them towards each other by ~0.16 Å (Filut et al., 1985); thus the distance between Ba^{2+} and OH^- is greater than the distance between Ba^{2+} and S^{2-}, due to repulsion from H^+. For sulfur in serpentine, a similar theory is suggested, in that an attraction between the SO_4^{2-} ions in the tetrahedra and the cations (Fe^{2+}, Mg^{2+}, Fe^{3+}) in the octahedra may cause a reduction in lattice spacings between the T-O layers. The partial replacement of OH^- by SH^- is, however, unlikely to cause a noticeable difference in lattice spacing distances. Though there is a difference in polarity between OH^- and SH^- due to oxygen being more electronegative than sulfur, the repulsion between the T-O layers caused by H^+ would be of similar, if not the same, magnitude. However, we note that this relationship was only determined to be statistically significant ($R = -0.963$) for Winchcombe and further work is needed to establish the significance in other samples.

The sequestration of sulfur in serpentine, rather than as sulfates such as gypsum, $CaSO_4$, may also be related to the prior formation of carbonates and thus a geochemical deficit of Ca and Mg in subsequent alteration fluids. The initial Ca and Mg budget available has been fixed as carbonates during the carbonation of ferromagnesian silicates during parent body alteration, as evidenced by the presence of carbonates in the CM and CI chondrites (de Leuw et al., 2010; Johnson & Prinz, 1993; Lee et al., 2014) including the samples studied here.

The presence of both S^{2-} and SO_4^{2-} implies a charge imbalance between the T-O layers in serpentine; however, this would be mitigated by the inclusion of ferric iron, Fe^{3+}, in the tetrahedral and octahedral sites, as identified via our Fe-K edge XANES results (Table 1 and Supporting Information S3). The nature of serpentine in CCs as being ferric serpentine is shown in our Fe-K XANES and is documented elsewhere (e.g., Buseck & Hua, 1993; Calvin & King, 1997; Elmaleh et al., 2015; Suttle et al., 2021; Tomeoka & Buseck, 1985, 1988; Velbel & Palmer, 2011; Zega et al., 2006), thus the inclusion of Fe^{3+} in our samples is expected.

Further analyses to determine the sulfur valences in Ryugu and related specimens (e.g., Bennu) would include energy-loss spectroscopy (EELS) and electron ptychography for establishing site occupancies, which would be techniques suitable for analyzing TEM lamella. To fully characterize the location and bonding environment of sulfur in serpentine, further work using X-ray diffraction (XRD), Extended X-ray Absorption Fine Structure spectroscopy (EXAFS), nano-Fourier Transform Infrared spectroscopy (nano-FTIR) and tip-enhanced Raman spectroscopy techniques will be useful for identifying and characterizing bond lengths in the material. Though the structural observations presented here are a good baseline comparison for the sulfur-bearing serpentine, a full structural solution is also needed, using techniques such as nanodiffraction and/or electron ptychography, along with those suggested above for determining the bonding environment.

Source of Sulfur for Serpentine

Alteration of Primary Sulfides

The parent bodies of CM and CI chondrites underwent widespread alteration (Bischoff, 1998; King et al., 2017, 2022; McSween, 1987; Rubin et al., 2007; Suttle et al., 2021; Takir et al., 2013) leading to the formation of secondary mineral assemblages. Fluid interactions caused alteration of primary minerals such as ferromagnesian silicates olivine and pyroxene, and of iron sulfides via oxidation. During serpentinization of Fe endmembers of olivine and pyroxene (fayalite and ferrosilite, respectively), Fe^{3+} ions are produced. Simultaneously, the serpentinization of Mg endmembers (forsterite and enstatite, respectively) led to some of the ferric Fe^{3+} ions being sequestered in the serpentine, forming ferric-serpentine. In Bassez (2017), it is inferred from enthalpy calculations that the oxidation of iron sulfides can proceed simultaneously with the oxidation (and carbonation) of ferromagnesian silicates during serpentinization. We propose that during parent body alteration there is concurrent oxidation of ferromagnesian silicates and iron sulfides, during which the sequestration of sulfur in serpentine takes place.

It is likely that the sulfur found in serpentine became available during the alteration of primary sulfides, as described in Singerling and Brearley (2018, 2020) and Singerling et al. (2024), 2024 eventually leading to the formation of magnetites. There are two key equations which are considered for the source of sulfur:

Alteration of pyrrhotite to magnetite:

$$3Fe_{1-x}S_{(s)} + 4H_2O_{(l)} \rightarrow Fe_3O_4 + 3HS^-_{(aq)} + 5H^+_{(aq)} + 2e^-_{(aq)} \quad (1)$$

Alteration of pentlandite to magnetite:

$$2Fe_{4.5}Ni_{4.5}S_{8(s)} + 7.5O_{2(aq)} + 6H^+{}_{(aq)} \rightarrow 3Fe^{2+}Fe^{3+}{}_2O_{4(s)} + 9Ni^{2+}{}_{(aq)} + 16S^{2-}{}_{(aq)} + 3H_2O_{(l)} \quad (2)$$

Equations (1) and (2) demonstrate two sources for the reduced sulfur species, as HS^- and S^{2-}. As these ions are in aqueous solution, it is likely that they were part of the wider fluid circulation on the parent body during alteration. Equation (2) further illustrates that the system must have been oxidizing, as in order to form magnetite from pentlandite, the pentlandite gains O_2 but loses Ni^{2+} and S^{2-} ions (Singerling et al., 2024). The remaining HS^- product from Equation (1), if not sequestered in serpentine, can form sulfate as oxidation of the parent body progresses (Zolotov, 2016), providing a potential source of sulfate ions for the serpentine:

$$HS^-{}_{(aq)} + 4H_2O_{(l)} \rightarrow SO_4{}^{2-}{}_{(aq)} + H^+{}_{(aq)} + 4H_{2(aq)} \quad (3)$$

For Equation (3) to occur, temperatures of ~150–200°C are required (Bassez, 2017; Zolotov, 2016). It has previously been shown that alteration temperatures on both the CM (Brearley, 2006; Clayton & Mayeda, 1984; Fujiya, 2018; King et al., 2021, 2022) and the CI (Brearley, 2006; Clayton & Mayeda, 1999; King et al., 2015) chondrites did reach ~150°C, a temperature high enough for Equation (3) to take place. In the CM chondrites, HS^- and $SO_4{}^{2-}$ are the "most probable and stable" (Singerling and Brearley, 2020) species observed under the oxygen fugacity fO_2 and pH 7–14 conditions on the CM parent body (see Figure 15 of Singerling and Brearley, 2020).

Pignatelli et al. (2016) also suggest that the alteration of primary troilite and other sulfides releases the sulfur needed for the S-rich fluid which allowed for the formation of tochilinite for both Type I and Type II TCIs; thus, it is plausible that the same fluid allowed for the formation of sulfur-bearing serpentine.

During aqueous alteration of these primary sulfides, metals and anhydrous silicates, TCIs and TCI-like material precipitated out and as alteration progressed, these TCIs were altered further and reprocessed to form phyllosilicates and secondary sulfides (Howard et al., 2009; Pignatelli et al., 2016, 2017; Rubin et al., 2007; Suttle et al., 2021; Tomeoka et al., 1989). Howard et al. (2009, and references therein) detail the chemical reactions in which tochilinite forms from primary metals (kamacite) and a S-rich fluid: the final products after continued tochilinite consumption are Mg- serpentines and Fe, Ni sulfides. Our suggested alteration sequence is in agreement with the equations described by Howard et al. (2009); however, we additionally suggest that these interactions are not sequential but are contemporaneous with each other. We also suggest that as part of the reprocessing of TCIs (particularly Type II) and TCI-like material, sulfur-bearing serpentine may form as an intermediate mineral phase, and/or sulfur-bearing serpentine remains or is (re)formed as a final alteration product alongside Mg phyllosilicates and secondary Fe, Ni sulfides and that the sulfur is not all sequestered in the sulfides.

The presence of sulfur associated with phyllosilicates has been previously reported by Brearley (2011), Singerling and Brearley (2020) and Singerling et al. (2024), where they note that a "fibrous oxysulfide" has formed alongside altered pyrrhotite-pentlandite intergrowth (PPI) grains and suggest this is one stage as part of the wider alteration of primary sulfides. According to Equation (2), an S^{2-}-rich fluid is present

and the sulfur must have a geochemical sink; thus there is potential for fluid flow elsewhere to form the fibrous oxysulfides, or, as we have identified, sulfur-bearing serpentine. It is noted that aside from the inclusions of micrometer-sized grains of pyrrhotite in the fibrous oxysulfide and the large sulfide grains around which it forms (Brearley, 2011), at the sub-micrometer level, the sulfur-bearing serpentines identified here and the oxysulfide have similar textures and appearance.

However, not all of the sulfur may necessarily be sequestered in serpentine via the partial replacement of OH^- and SO_4^{2-} ions; some sulfur may have been lost via other processes, such as volatile loss. This is also suggested by Singerling and Brearley (2018) as they observed variable sulfur content in the final sulfide products of alteration in the CMs, assuming some sulfur is lost as volatiles. However, we suggest it is possible that some sulfur content variability is due to a range of sulfur sequestration in serpentine.

Research on the CI chondrites (e.g., Buseck & Hua, 1993; Tomeoka & Buseck, 1988) states that ferrihydrite is present in equal proportions to, and mixed in with, the phyllosilicates. The fine-grained nature of the ferrihydrite led to adsorption of sulfur (and other volatiles) onto its surface, which could explain the high sulfur content seen in CI chondrite matrices (Buseck & Hua, 1993). However, the ferrihydrite is distinctly different from the phyllosilicate matrix, as observed with BSE imaging where the ferrihydrite appears much brighter than the matrix materials, and with EDS measurements which show compositional differences between the two mineral phases. Thus, adsorption of sulfur to the ferrihydrite cannot explain the sulfur content in the CI phyllosilicate matrix, as observed with STEM-EDS measurements in this work on Ivuna, where ferrihydrite was not detected.

Tomeoka and Buseck (1988) suggest a sulfate-rich solution was responsible for the presence of sulfur on ferrihydrite and that this period of alteration occurred simultaneously with sulfate vein formation. Although the sulfur seen in the CIs in this work has been identified as S^{6+}, thus agreeing with the conclusions of Tomeoka and Buseck (1988) regarding the presence of sulfate, we propose the sulfur is not just adsorbed to ferrihydrite surfaces but is trapped in the matrix serpentines as SO_4^{2-} ions, as discussed in Sulfur in Carbonaceous Chondrites Section. The presence of sulfur in its most oxidized state, S^{6+}, and the abundance of magnetites seen in the CIs (Alfing et al., 2019; Hyman & Rowe, 1983; King et al., 2015) imply that the CI chondrites experienced a more advanced degree of oxidation than the CMs. From Equation (3) and in the works of Singerling and Brearley (2020) and Singerling et al., (2024) the products that form at the most advanced stages of oxidation of primary minerals (notably, iron sulfides) and their subsequent products, are sulfates and magnetite. It is widely agreed within the literature (Bischoff, 1998; King et al., 2015; Suttle et al., 2019) that the CIs experienced more alteration than the CMs, and the largest degree of alteration of all CCs, thus explaining the abundances of S^{6+} and magnetite in these specimens. It is, however, crucial to note that any alteration within the CIs, especially in the case of Orgueil, the effects of terrestrial weathering need to be considered.

Less sulfur is observed in the S^{2-} state (as S^{2-} in sulfur-bearing serpentine) in the CIs, which could be attributed to the fact that they have experienced the most aqueous alteration on their parent bodies. Sulfur-bearing serpentine is likely an intermediate step in the alteration process; thus the CMs contain more of this mineral as they have experienced less alteration compared to the CIs. In the CIs, it is possible that a large amount of the sulfur has been re-consumed as part of the cycling of sulfur within the alteration process, forming tochilinite and TCIs from sulfur-bearing serpentine and progressing further to form sulfides and finally, magnetite. This also fits with the number of micro and nanoscale magnetite grains that are observed in the CI chondrites and CI-like carbonaceous asteroid samples.

Implications for the Sulfur Cycle

The terrestrial sulfur cycle is important in bio- and geochemical processes; the global cycling of sulfur through different oxidation states produces species of varying valency, which play important roles in both geological and biological systems. The sulfur content (normalized relative to Si) of CI chondrites has a 1:1 correspondence to that of the solar photosphere (Anders & Grevesse, 1989); thus, the bulk meteoritic sulfur content is a reasonable approximation for the bulk planetary sulfur abundance. The CM chondrites have a similar photosphere correspondence to the CIs; however, they are depleted in volatile elements, $\sim 0.63 \times$ CI, and have some enrichment of refractory elements, $\sim 1.2 \times$ CI (Bland et al., 2005; Braukmüller et al., 2018; Suttle et al., 2021). Both are considered to be likely candidates for the starting materials for the formation of the rocky inner planets in the early Solar System.

As approximately 15% of phyllosilicates identified in Winchcombe are sulfur-bearing serpentine, and the bulk volume of CM and CI chondrites is largely phyllosilicate material, then phyllosilicates can play a key, previously unidentified role in the sulfur cycle and distribution of volatiles in the early Solar System.

CONCLUSIONS

Correlative multi-technique structural and compositional analyses at μm–nm scales of Winchcombe

(CM2), Aguas Zarcas (CM2), Ivuna (CI), Orgueil (CI) and Ryugu have revealed that sulfur-bearing serpentines are an important component of these samples. In Winchcombe, 12 vol% of the sectioned studied here is sulfur-bearing serpentine, with sulfur abundance up to 10 wt% SO_3 equivalent. There are similar abundances noted in the other samples, averaging 15 wt% in Aguas Zarcas, 15 wt% in Ivuna and Orgueil, and 6 wt% in Ryugu (all SO_3 equivalent). On the basis of our studies, we conclude that much of the material identified in previous studies of CCs as TCI-like or PCPs is in fact sulfur-bearing serpentine.

Fourier-filtered HRTEM measurments determinedthe d_{001}-spacings were 0.64–0.70 nm across all sulfur-bearing serpentine sites in Winchcombe. The average d_{001}-spacings for both the CMs and the CIs were equal to 0.68 ± 0.02 nm. In Winchcombe, we were able to identify an anti-correlation between these basal lattice spacings and sulfur abundance. We suggest that the attraction between the S^{2-} (in HS^- species) or SO_4^{2-} and the Fe^{2+} in the octahedral sites may cause a reduction in lattice spacings between the T-O layers. Thus far, we have only positively identified this anti-correlation in Winchcombe.

On the basis of our S-K edge XANES analyses we determine that sulfur is in the form S^{2-} (forming part of an HS^- species) and S^{6+}, that is, (SO_4^{2-}). CM sulfur-bearing serpentines have $S^{6+}/\Sigma S_{total}$ values of 0.1–0.2 and S^{2-} as the dominant species, whereas the CIs have values of 0.9–1.0 with S^{6+} as the dominant species. On the basis of our combined analyses we suggest that sulfur-bearing, ferric serpentine has an approximate mineral formula $(Mg, Fe^{2+}, Fe^{3+}, Al)_{2\text{-}3}(Si, Al)_2O_5(OH)_{5\text{-}6}(HS^-)_{1\text{-}2}(SO_4)^{2-}_{0.1\text{-}0.7}$. Fe-K XANES confirm the ferric abundances of around 50% ($Fe^{3+}/\Sigma Fe = \sim 0.5$).

It is possible that sulfur-bearing serpentine is an intermediate product that forms as part of the progressive aqueous alteration that occurred on CC parent bodies. A sulfur-rich fluid formed part of the wider alteration pathway, and during alteration, there was simultaneous oxidation of ferromagnesian silicates and Fe-sulfides, during which sulfur was variably sequestered in serpentine.

The heterogeneity observed in both sulfur-bearing serpentine abundance and differing morphologies may be explained by the varying degrees of aqueous alteration, and thus oxidation, across the CMs and CIs. Sulfur-bearing serpentines that were once present in CI precursor material may have been re-consumed as part of the extensive alteration, recycling of sulfur and the formation of secondary sulfides and magnetite on CI parent asteroid(s).

As sulfur-bearing serpentine has a variable and sometimes, as in Winchcombe, a large abundance, we conclude that a significant amount of sulfur is sequestered in serpentines within CM and CI chondrite material and related asteroids. Thus, we suggest that phyllosilicates and in particular serpentine, had a previously unrecognized important role in the sulfur cycle of the early Solar System.

Acknowledgments—The authors thank Mike Zolensky and the two anonymous reviewers for their constructive feedback on this manuscript. We thank Diamond Light Source for access and support in the use of ePSIC (proposals MG30752, MG31953, MG32874, MG35976) and beamline I18 (proposals SP29615-1, SP31641-1, SP35046-1). The ePSIC team, in particular, Dr Christopher Allen and Dr Jinseok Ryu, are thanked for their assistance with all ePSIC analyses, especially with 4D STEM. Dr Konstantin Ignatyev (Beamline I18) is thanked for help with the synchrotron analyses for sessions SP29615-1 (June 2021) and SP31641-1 (April 2022) for Fe-K XANES measurements, and especially for his efforts throughout the COVID-19 lockdown and allowing the authors remote access to the beamline controls. Dr Tina Geraki and the I18 beamline staff are thanked for their assistance with session SP35046-1 (December 2023) for S-K XANES. The Natural History Museum London is thanked for loans of Winchcombe P30543, Ivuna P12628 and Orgueil P16061/BM.1985, M148. The JAXA Hayabusa2 team is thanked for loans of Ryugu samples C0105-035_000_00, A0058-C2001_08, A0104-017_006_02. Dr Michael Fay is thanked for his help with analyses at the University of Nottingham nmRC. Dr Annika Burns, UoL, is thanked for the preparation of the Aguas Zarcas thin section. The authors acknowledge the help and support of staff and microanalysis equipment at the Advanced Microscopy Facility UoL, and the Hercules Facility at UoL, supported by EPSRC grant EP/X014614/1. STFC is thanked for funding Niamh Topping's PhD studentship. This research was funded in whole or in part by STFC. For the purpose of Open Access, the authors have applied a CC BY public copyright license to the Accepted Manuscript version arising from this submission.

Data Availability Statement—The data that support the findings of this study are available from the corresponding author upon reasonable request.

Editorial Handling—Dr. Michael Zolensky

REFERENCES

Aléon-Toppani, A., Brunetto, R., Dionnet, Z., Rubino, S., Baklouti, D., Brisset, F., Vallet, M., et al. 2024. Correlated IR-SEM-TEM Studies of Three Different Grains from

Ryugu: From the Initial Material to Post-Accretional Processes. *Geochimica et Cosmochimica Acta* 371: 1–30.

Alexander, C. M. O. D., Wynn, J. G., and Bowden, R. 2022. Sulfur Abundances and Isotopic Compositions in Bulk Carbonaceous Chondrites and Insoluble Organic Material: Clues to Elemental and Isotopic Fractionations of Volatile Chalcophiles. *Meteoritics & Planetary Science* 57: 334–351.

Alfing, J., Patzek, M., and Bischoff, A. 2019. Modal Abundances of Coarse-Grained (>5 µm) Components within CI-Chondrites and their Individual Clasts—Mixing of Various Lithologies on the CI Parent Body(Ies). *Geochemistry* 79: 125532.

Anders, E., and Grevesse, N. 1989. Abundances of the Elements: Meteoritic and Solar. *Geochimica et Cosmochimica Acta* 53(1): 197–214.

Anzures, B. A., Parman, S. W., Milliken, R. E., Lanzirotti, A., and Newville, M. 2020. XANES Spectroscopy of Sulfides Stable under Reducing Conditions. *American Mineralogist* 105: 375–381.

Arai, T., Suzuki, K., Moriwaki, R., and Matsui, T. 2022. Carbon and Sulfur Abundances in Carbonaceous Meteorites Revisited. In NIPR 13th Symposium on Polar Science, Tokyo, Japan.

Bassez, M.-P. 2017. Anoxic and Oxic Oxidation of Rocks Containing Fe(II)Mg-Silicates and Fe(II)-Monosulfides as Source of Fe(III)-Minerals and Hydrogen. Geobiotropy. *Origins of Life and Evolution of Biospheres* 47: 453–480.

Bates, H. C., King, A. J., Donaldson Hanna, K. L., Bowles, N. E., and Russell, S. S. 2020. Linking Mineralogy and Spectroscopy of Highly Aqueously Altered CM and CI Carbonaceous Chondrites in Preparation for Primitive Asteroid Sample Return. *Meteoritics & Planetary Science* 55: 77–101.

Bates, H. C., King, A. J., Shirley, K. S., Bonsall, E., Schröder, C., Wombacher, F., Fockenberg, T., Curtis, R. J., and Bowles, N. E. 2024. The Bulk Mineralogy, Elemental Composition, and Water Content of the Winchcombe CM Chondrite Fall. *Meteoritics & Planetary Science* 59: 1006–28.

Bischoff, A. 1998. Aqueous Alteration of Carbonaceous Chondrites: Evidence for Preaccretionary Alteration—A Review. *Meteoritics & Planetary Science* 33: 1113–22.

Bland, P. A., Alard, O., Benedix, G. K., Kearsley, A. T., Menzies, O. N., Watt, L. E., and Rogers, N. W. 2005. Volatile Fractionation in the Early Solar System and Chondrule/Matrix Complementarity. *Proceedings of the National Academy of Sciences* 102: 13755–60.

Braukmüller, N., Wombacher, F., Funk, C., and Münker, C. 2019. Earth's Volatile Element Depletion Pattern Inherited from a Carbonaceous Chondrite-like Source. *Nature Geoscience* 12: 564–68.

Braukmüller, N., Wombacher, F., Hezel, D. C., Escoube, R., and Münker, C. 2018. The Chemical Composition of Carbonaceous Chondrites: Implications for Volatile Element Depletion, Complementarity and Alteration. *Geochimica et Cosmochimica Acta* 239: 17–48.

Brearley, A. J. 2006. The Action of Water. In *Meteorites and the Early Solar System II*, edited by D. S. Lauretta, and H. Y. McSween, Jr., 587–624. Tucson: University of Arizona Press.

Brearley, A. J. 2011. Alteration of Coarse-Grained Fe and Fe, Ni Sulfides in the Mighei CM2 Carbonaceous Chondrite: Evidence for the Instability of Primary Pyrrhotite-Pentlandite Grains during Aqueous Alteration 42nd Lunar and Planetary Science Conference, Abstract #2233. Lunar and Planetary Institute, Houston.

Brearley, A. J., Barnes, J. D., and Sharp, Z. D. 2007. Chrysotile Nanotubes: Potential Host of Insoluble Chlorine in Serpentinized Oceanic Crust Abstracts of AGU Fall Meeting. #V11E-04.

Brearley, A. J., and Jones, R. H. 1998. Chondritic Meteorites. *Reviews in Mineralogy and Geochemistry* 36: 3-01–3-398.

Brindley, G. W., and Brown, G. 1984. *Crystal Structures of Clay Minerals and Their X-ray Identification*. London: Mineralogical Society.

Brosnan, J. T., and Brosnan, M. E. 2006. The Sulfur-Containing Amino Acids: An Overview12. *The Journal of Nutrition* 136: 1636S–1640S.

Bullock, E. S., McKeegan, K. D., Gounelle, M., Grady, M. M., and Russell, S. S. 2010. Sulfur Isotopic Composition of Fe-Ni Sulfide Grains in CI and CM Carbonaceous Chondrites. *Meteoritics & Planetary Science* 45: 885–898.

Bunch, T. E., and Chang, S. 1980. Carbonaceous Chondrites —II. Carbonaceous Chondrite Phyllosilicates and Light Element Geochemistry as Indicators of Parent Body Processes and Surface Conditions. *Geochimica et Cosmochimica Acta* 44: 1543–77.

Burgess, R., Wright, I. P., and Pillinger, C. T. 1991. Determination of Sulphur-Bearing Components in C1 and C2 Carbonaceous Chondrites by Stepped Combustion. *Meteoritics* 26: 55–64.

Buseck, P. R., and Hua, X. 1993. Matrices of Carbonaceous Chondrite Meteorites. *Annual Review of Earth and Planetary Sciences* 21: 255–305.

Calvin, W. M., and King, T. V. V. 1997. Spectral Characteristics of Iron-Bearing Phyllosilicates: Comparison to Orgueil (CI1), Murchison and Murray (CM2). *Meteoritics & Planetary Science* 32: 693–701.

Changela, H. G., Kebukawa, Y., Petera, L., Ferus, M., Chatzitheodoridis, E., Nejdl, L., Nebel, R., et al. 2024. The Evolution of Organic Material on Asteroid 162173 Ryugu and its Delivery to Earth. *Nature Communications* 15(1): 6165.

Charlson, R. J., Anderson, T. L., and McDuff, R. E. 2000. The sulfur cycle. In *Earth system science: From biogeochemical cycles to global change*, edited by M. C. Jacobson, R. J. Charlson, H. Rodhe, and G. H. Orians, 343–359. San Diego, CA: Elsevier.

Clayton, R. N., and Mayeda, T. K. 1984. The Oxygen Isotope Record in Murchison and Other Carbonaceous Chondrites. *Earth and Planetary Science Letters* 67: 151–161.

Clayton, R. N., and Mayeda, T. K. 1999. Oxygen Isotope Studies of Carbonaceous Chondrites. *Geochimica et Cosmochimica Acta* 63: 2089–2104.

Daly, L., Lee, M. R., Bagot, P., Halpin, J., Smith, W., McFadzean, S., O'Brien, A. C., Griffin, S., Hallis, L. J., and Cohen, B. E. 2020. Exploring Mars at the Nanoscale: Applications of Transmission Electron Microscopy and Atom Probe Tomography in Planetary Exploration. *IOP Conference Series: Materials Science and Engineering* 891: 12008.

Daly, L., Suttle, M. D., Lee, M. R., Bridges, J., Hicks, L., Martin, P.-E. M. C., Floyd, C. J., et al. 2024. Brecciation at the Grain Scale within the Lithologies of the Winchcombe Mighei-like Carbonaceous Chondrite. *Meteoritics & Planetary Science* 59: 1068–1100.

de la Peña, F., Ostasevicius, T., Fauske, V. T., Burdet, P., Prestat, E., Jokubauskas, P., Nord, M., et al. 2024. hyperspy/hyperspy: v2.2.0 In *Zenodo*.

de Leuw, S., Rubin, A. E., and Wasson, J. T. 2010. Carbonates in CM Chondrites: Complex Formational Histories and Comparison to Carbonates in CI Chondrites. *Meteoritics & Planetary Science* 45: 513–530.

Debret, B., Andreani, M., Delacour, A., Rouméjon, S., Trcera, N., and Williams, H. 2017. Assessing Sulfur Redox State and Distribution in Abyssal Serpentinites Using XANES Spectroscopy. *Earth and Planetary Science Letters* 466: 1–11.

Deer, W. A., Howie, R. A., and Zussman, J. 1992. *An Introduction to the Rock-Forming Minerals*, 2nd ed. Harlow: Longman Scientific & Technical.

Dreibus, G., Palme, H., Spettel, B., Zipfel, J., and Wänke, H. 1995. Sulfur and Selenium in Chondritic Meteorites. *Meteoritics* 30: 439–445.

Elmaleh, A., Bourdelle, F., Caste, F., Benzerara, K., Leroux, H., and Devouard, B. 2015. Formation and Transformations of Fe-Rich Serpentines by Asteroidal Aqueous Alteration Processes: A Nanoscale Study of the Murray Chondrite. *Geochimica et Cosmochimica Acta* 158: 162–178.

European Synchrotron Radiation Facility (ESRF). 2018. ID21 Sulfur XANES Spectra Database. Database Inorganic Sulfur Compounds Accessed 15 May 2024. https://www.esrf.fr/home/UsersAndScience/Experiments/XNP/ID21/php/Database-SCompounds.html.

Feuillie, C., Daniel, I., Michot, L. J., and Pedreira-Segade, U. 2013. Adsorption of Nucleotides onto Fe–Mg–Al Rich Swelling Clays. *Geochimica et Cosmochimica Acta* 120: 97–108.

Filut, M. A., Rule, A. C., and Bailey, S. W. 1985. Crystal Structure Refinement of Anandite-2Or, a Barium- and Sulphur-Bearing Trioctahedral Mica. *American Mineralogist* 70: 1298–1308.

Fleet, M. E. 2005. XANES Spectroscopy of Sulfur in Earth Materials. *The Canadian Mineralogist* 43: 1811–38.

Fuchs, L. H., Olsen, E. J., and Jensen, K. J. 1973. Mineralogy, Mineral-Chemistry, and Composition of the Murchison (C2) Meteorite. In *Smithsonian Contributions to the Earth Sciences*, 1–39. Washington: Smithsonian Institution Press.

Fujiya, W. 2018. Oxygen Isotopic Ratios of Primordial Water in Carbonaceous Chondrites. *Earth and Planetary Science Letters* 481: 264–272.

Garvie, L. A. J. 2021. Mineralogy of the 2019 Aguas Zarcas (CM2) Carbonaceous Chondrite Meteorite Fall. *American Mineralogist* 106: 1900–1916.

Gounelle, M., and Zolensky, M. E. 2001. A Terrestrial Origin for Sulfate Veins in CI1 Chondrites. *Meteoritics & Planetary Science* 36: 1321–29.

Gounelle, M., and Zolensky, M. E. 2014. The Orgueil Meteorite: 150 Years of History. *Meteoritics & Planetary Science* 49: 1769–94.

Hassan, I., and Grundy, H. D. 1991. The Crystal Structure of Hauyne at 293 and 153 K. *The Canadian Mineralogist* 29: 123–130.

Hicks, L. J. 2015. X-Ray Spectroscopy and Electron Microscopy of Planetary Materials. Thesis. Department of Physics and Astronomy, University of Leicester Accessed 4 March 2025. https://lra.le.ac.uk/handle/2381/31986.

Hicks, L. J., Bridges, J. C., and Gurman, S. 2014. Ferric Saponite and Serpentine in the Nakhlite Martian Meteorites. *Geochimica et Cosmochimica Acta* 136: 194–210.

Howard, K. T., Alexander, C. M. O. D., Schrader, D. L., and Dyl, K. A. 2015. Classification of Hydrous Meteorites (CR, CM and C2 Ungrouped) by Phyllosilicate Fraction: PSD-XRD Modal Mineralogy and Planetesimal Environments. *Geochimica et Cosmochimica Acta* 149: 206–222.

Howard, K. T., Benedix, G. K., Bland, P. A., and Cressey, G. 2009. Modal Mineralogy of CM2 Chondrites by X-Ray Diffraction (PSD-XRD). Part 1: Total Phyllosilicate Abundance and the Degree of Aqueous Alteration. *Geochimica et Cosmochimica Acta* 73: 4576–89.

Hyman, M., and Rowe, M. W. 1983. Magnetite in CI Chondrites. *Journal of Geophysical Research: Solid Earth* 88(S02): A736–A740.

Ito, M., Tomioka, N., Uesugi, M., Yamaguchi, A., Shirai, N., Ohigashi, T., Liu, M.-C., Greenwood, R. C., Kimura, M., et al. 2022. A Pristine Record of Outer Solar System Materials from Asteroid Ryugu's Returned Sample. *Nature Astronomy* 6: 1163–71.

Johnson, C. A., and Prinz, M. 1993. Carbonate Compositions in CM and CI Chondrites and Implications for Aqueous Alteration. *Geochimica et Cosmochimica Acta* 57: 2843–52.

Jørgensen, B. B., Findlay, A. J., and Pellerin, A. 2019. The Biogeochemical Sulfur Cycle of Marine Sediments. *Frontiers in Microbiology* 10: 1–27.

Kerraouch, I., Bischoff, A., Zolensky, M. E., Pack, A., Patzek, M., Hanna, R. D., Fries, M. D., et al. 2021. The Polymict Carbonaceous Breccia Aguas Zarcas: A Potential Analog to Samples Being Returned by the OSIRIS-REx and Hayabusa2 Missions. *Meteoritics & Planetary Science* 56: 277–310.

King, A. J., Daly, L., Rowe, J., Joy, K. H., Greenwood, R. C., Devillepoix, H. A. R., Suttle, M. D., Chan, Q. H. S., et al. 2022. The Winchcombe Meteorite, a Unique and Pristine Witness from the Outer Solar System. *Science Advances* 8: eabq3925.

King, A. J., Phillips, K. J. H., Strekopytov, S., Vita-Finzi, C., and Russell, S. S. 2020. Terrestrial Modification of the Ivuna Meteorite and a Reassessment of the Chemical Composition of the CI Type Specimen. *Geochimica et Cosmochimica Acta* 268: 73–89.

King, A. J., Schofield, P. F., Howard, K. T., and Russell, S. S. 2015. Modal Mineralogy of CI and CI-like Chondrites by X-Ray Diffraction. *Geochimica et Cosmochimica Acta* 165: 148–160.

King, A. J., Schofield, P. F., and Russell, S. S. 2017. Type 1 Aqueous Alteration in CM Carbonaceous Chondrites: Implications for the Evolution of Water-Rich Asteroids. *Meteoritics & Planetary Science* 52: 1197–1215.

King, A. J., Schofield, P. F., and Russell, S. S. 2021. Thermal Alteration of CM Carbonaceous Chondrites: Mineralogical Changes and Metamorphic Temperatures. *Geochimica et Cosmochimica Acta* 298: 167–190.

King, A. J., Tu, V., Schofield, P. F., Najorka, J., Russell, S. S., Bates, H. C., Zega, T. J., et al. 2024. The Mineralogy of Asteroid Bennu: First Results from X-Ray Powder Diffraction of Returned Samples. In *55th Lunar and Planetary Science Conference*, 1109. Houston: Lunar and Planetary Institute.

Krämer Ruggiu, L., Devouard, B., Gattacceca, J., Bonal, L., Leroux, H., Eschrig, J., Borschneck, D., et al. 2022. Detection of Incipient Aqueous Alteration in Carbonaceous Chondrites. *Geochimica et Cosmochimica Acta* 336: 308–331.

Lauretta, D. S., Hua, X., and Buseck, P. R. 2000. Mineralogy of Fine-Grained Rims in the Alh 81002 cm Chondrite. *Geochimica et Cosmochimica Acta* 64: 3263–73.

Lee, M. R., Bland, P. A., and Graham, G. 2003. Preparation of TEM Samples by Focused Ion Beam (FIB) Techniques: applications to the Study of Clays and Phyllosilicates in Meteorites. *Mineralogical Magazine* 67: 581–592.

Lee, M. R., and Greenwood, R. C. 1994. Alteration of Calcium- and Aluminium-rich Inclusions in the Murray (CM2) Carbonaceous Chondrite. *Meteoritics* 29: 780–790.

Lee, M. R., Lindgren, P., and Sofe, M. R. 2014. Aragonite, Breunnerite, Calcite and Dolomite in the CM Carbonaceous Chondrites: High Fidelity Recorders of Progressive Parent Body Aqueous Alteration. *Geochimica et Cosmochimica Acta* 144: 126–156.

Lee, M. R., Sofe, M. R., Lindgren, P., Starkey, N. A., and Franchi, I. A. 2013. The Oxygen Isotope Evolution of Parent Body Aqueous Solutions as Recorded by Multiple Carbonate Generations in the Lonewolf Nunataks 94101 CM2 Carbonaceous Chondrite. *Geochimica et Cosmochimica Acta* 121: 452–466.

Lentfort, S., Bischoff, A., Ebert, S., and Patzek, M. 2021. Classification of CM Chondrite Breccias—Implications for the Evaluation of Samples from the OSIRIS-REx and Hayabusa 2 Missions. *Meteoritics & Planetary Science* 56: 127–147.

Lerner, A. H., Muth, M. J., Wallace, P. J., Lanzirotti, A., Newville, M., Gaetani, G. A., Chowdhury, P., and Dasgupta, R. 2021. Improving the Reliability of Fe- and S-XANES Measurements in Silicate Glasses: Correcting Beam Damage and Identifying Fe-Oxide Nanolites in Hydrous and Anhydrous Melt Inclusions. *Chemical Geology* 586: 120610.

Mackinnon, I. D. R., and Zolensky, M. E. 1984. Proposed Structures for Poorly Characterized Phases in C2M Carbonaceous Chondrite Meteorites. *Nature* 309: 240–42.

McSween, H. Y. 1987. Aqueous Alteration in Carbonaceous Chondrites: Mass Balance Constraints on Matrix Mineralogy. *Geochimica et Cosmochimica Acta* 51: 2469–77.

Mellini, M. 1982. The Crystal Structure of Lizardite 1T: hydrogen Bonds and Polytypism. *American Mineralogist* 67: 587–598.

Mellini, M., Cressey, G., Wicks, F. J., and Cressey, B. A. 2010. The Crystal Structure of Mg End-Member Lizardite-1T Forming Polyhedral Spheres from the Lizard, Cornwall. *Mineralogical Magazine* 74: 277–284.

Metzler, K., Bischoff, A., and Stöffler, D. 1992. Accretionary Dust Mantles in CM Chondrites: Evidence for Solar Nebula Processes. *Geochimica et Cosmochimica Acta* 56: 2873–97.

Momma, K., and Izumi, F. 2011. VESTA 3 for Three-Dimensional Visualization of Crystal, Volumetric and Morphology Data. *Journal of Applied Crystallography* 44: 1272–76.

Nakamura, T., and Nakamuta, Y. 1996. X-ray study of PCP from the Murchison CM carbonaceous chondrite. *Proceedings of the NIPR Symposium on Antarctic Meteorites* 9: 37–50.

Nakamura, E., Kobayashi, K., Tanaka, R., Kunihiro, T., Kitagawa, H., Potiszil, C., Ota, T., Sakaguchi, C., et al. 2022. On the Origin and Evolution of the Asteroid Ryugu: A Comprehensive Geochemical Perspective. *Proceedings of the Japan Academy, Series B* 98: 227–282.

Nakamura, T., Matsumoto, M., Amano, K., Enokido, Y., Zolensky, M. E., Mikouchi, T., Genda, H., et al. 2023. Formation and Evolution of Carbonaceous Asteroid Ryugu: Direct Evidence from Returned Samples. *Science* 379: eabn8671.

Naraoka, H., Hashiguchi, M., and Okazaki, R. 2023. Soluble Sulfur-Bearing Organic Compounds in Carbonaceous Meteorites: Implications for Chemical Evolution in Primitive Asteroids. *ACS Earth and Space Chemistry* 7: 41–48.

Noguchi, T., Matsumoto, T., Miyake, A., Igami, Y., Haruta, M., Saito, H., Hata, S., et al. 2023. A Dehydrated Space-Weathered Skin Cloaking the Hydrated Interior of Ryugu. *Nature Astronomy* 7: 170–181.

Ophus, C. 2019. Four-Dimensional Scanning Transmission Electron Microscopy (4D-STEM): From Scanning Nanodiffraction to Ptychography and beyond. *Microscopy and Microanalysis* 25: 563–582.

Ophus, C. 2023. Quantitative Scanning Transmission Electron Microscopy for Materials Science: Imaging, Diffraction, Spectroscopy, and Tomography. *Annual Review of Materials Research* 53: 105–141.

Organova, N. I., Drits, V. A., and Dmitrik, A. L. 1973. Structural Study of Tochilinite. Part I. The Isometric Variety. *Soviet Physics—Crystallography* 17: 667–671.

Palmer, E. E., and Lauretta, D. S. 2011. Aqueous Alteration of Kamacite in CM Chondrites. *Meteoritics & Planetary Science* 46: 1587–1607.

Pekov, I. V., Sereda, E. V., Polekhovsky, Y. S., Britvin, S. N., Chukanov, N. V., Yapaskurt, V. O., and Bryzgalov, I. A. 2013. Ferrotochilinite, 6FeS · 5Fe(OH)2, a New Mineral from the Oktyabr'sky Deposit, Noril'sk District, Siberia, Russia. *Geology of Ore Deposits* 55: 567–574.

Peng, Y., and Jing, Y. 2014. Hydrothermal Preparation of Analogous Matrix Minerals of CM Carbonaceous Chondrites from Metal Alloy Particles. *Earth and Planetary Science Letters* 408: 252–262.

Peng, Y., Xu, L., Xi, G., Zhong, C., Lu, J., Meng, Z., Li, G., Zhang, S., Zhang, G., and Qian, Y. 2007. An Experimental Study on the Hydrothermal Preparation of Tochilinite Nanotubes and Tochilinite–Serpentine-Intergrowth Nanotubes from Metal Particles. *Geochimica et Cosmochimica Acta* 71: 2858–75.

Petera, L., Changela, H., Bridges, J., Kebukawa, Y., Hicks, L., Topping, N., and Ferus, M. 2023. A Comparative Carbon XANES and EELS Study of Organic Matter in the Ivuna CI Chondrite EGU General Assembly 2023, Vienna, https://doi.org/10.5194/egusphere-egu23-14828.

Pignatelli, I., Marrocchi, Y., Mugnaioli, E., Bourdelle, F., and Gounelle, M. 2017. Mineralogical, Crystallographic and Redox Features of the Earliest Stages of Fluid Alteration in CM Chondrites. *Geochimica et Cosmochimica Acta* 209: 106–122.

Pignatelli, I., Marrocchi, Y., Vacher, L. G., Delon, R., and Gounelle, M. 2016. Multiple Precursors of Secondary Mineralogical Assemblages in CM Chondrites. *Meteoritics & Planetary Science* 51: 785–805.

Prange, A., Dahl, C., Trüper, H. G., Behnke, M., Hahn, J., Modrow, H., and Hormes, J. 2002. Investigation of S-H Bonds in Biologically Important Compounds by Sulfur K-Edge X-Ray Absorption Spectroscopy 20: 589–596.

Räisänen, J. 2005. Sulfur. In *Encyclopedia of Analytical Science*, edited by P. Worsfold, A. Townshend, and C. Poole, 2nd ed., 415–423. Oxford: Elsevier.

Ravel, B., and Newville, M. 2005. Athena, Artemis, Hephaestus: Data Analysis for X-Ray Absorption

Spectroscopy Using IFEFFIT. *Journal of Synchrotron Radiation* 12: 537–541.

Rubin, A. E., Trigo-Rodríguez, J. M., Huber, H., and Wasson, J. T. 2007. Progressive Aqueous Alteration of CM Carbonaceous Chondrites. *Geochimica et Cosmochimica Acta* 71: 2361–82.

Ryu, J., Kim, H., Kim, R. M., Kim, S., Jo, J., Lee, S., Nam, K. T., et al. 2021. Dimensionality Reduction and Unsupervised Clustering for EELS-SI. *Ultramicroscopy* 231: 113314.

Sapozhnikov, A. N., Chukanov, N. V., Shendrik, R. Y., Vigasina, M. F., Tauson, V. L., Lipko, S. V., Belakovskiy, D. I., Levitskii, V. I., Suvorova, L. F., and Ivanova, L. A. 2022. Lazurite: Validation as a Mineral Species with the Formula $Na_7Ca(Al_6Si_6O_{24})(SO_4)S_3$•- $\cdot H_2O$ and New Data. *Geology of Ore Deposits* 64: 470–75.

Savitzky, B. H., Zeltmann, S. E., Hughes, L. A., Brown, H. G., Zhao, S., Pelz, P. M., Pekin, T. C., et al. 2021. py4DSTEM: A Software Package for Four-Dimensional Scanning Transmission Electron Microscopy Data Analysis. *Microscopy and Microanalysis* 27: 712–743.

Schneider, C. A., Rasband, W. S., and Eliceiri, K. W. 2012. NIH Image to ImageJ: 25 Years of Image Analysis. *Nature Methods* 9: 671–75.

Schrader, D. L., Davidson, J., and McCoy, T. J. 2016. Widespread Evidence for High-Temperature Formation of Pentlandite in Chondrites. *Geochimica et Cosmochimica Acta* 189: 359–376.

Schrader, D. L., Davidson, J., McCoy, T. J., Zega, T. J., Russell, S. S., Domanik, K. J., and King, A. J. 2021. The Fe/S Ratio of Pyrrhotite Group Sulfides in Chondrites: An Indicator of Oxidation and Implications for Return Samples from Asteroids Ryugu and Bennu. *Geochimica et Cosmochimica Acta* 303: 66–91.

Sievert, S. M., Kiene, R. P., and Schulz-Vogt, H. N. 2007. The Sulfur Cycle. *Oceanography* 20: 117–123.

Singerling, S. A., and Brearley, A. J. 2018. Primary Iron Sulfides in CM and CR Carbonaceous Chondrites: Insights into Nebular Processes. *Meteoritics & Planetary Science* 53: 2078–2106.

Singerling, S. A., and Brearley, A. J. 2020. Altered Primary Iron Sulfides in CM2 and CR2 Carbonaceous Chondrites: Insights into Parent Body Processes. *Meteoritics & Planetary Science* 55: 496–523.

Singerling, S. A., Corrigan, C. M., and Brearley, A. J. 2024. The Fate of Primary Iron Sulfides in the CM1 Carbonaceous Chondrites: Effects of Advanced Aqueous Alteration on Primary Components. *Meteoritics & Planetary Science* 59: 475–501.

Suttle, M. D., Daly, L., Jones, R. H., Jenkins, L., van Ginneken, M., Mitchell, J. T., Bridges, J. C., Hicks, L. J., et al. 2024. The Winchcombe Meteorite—A Regolith Breccia from a Rubble Pile CM Chondrite Asteroid. *Meteoritics & Planetary Science* 59: 1043–67.

Suttle, M. D., Folco, L., Genge, M. J., Russell, S. S., Najorka, J., and van Ginneken, M. 2019. Intense Aqueous Alteration on C-Type Asteroids: Perspectives from Giant Fine-Grained Micrometeorites. *Geochimica et Cosmochimica Acta* 245: 352–373.

Suttle, M. D., King, A. J., Schofield, P. F., Bates, H., and Russell, S. S. 2021. The Aqueous Alteration of CM Chondrites, a Review. *Geochimica et Cosmochimica Acta* 299: 219–256.

Tachibana, S., Sawada, H., Okazaki, R., Takano, Y., Sakamoto, K., Miura, Y. N., Okamoto, C., et al. 2022. Pebbles and Sand on Asteroid (162173) Ryugu: In Situ Observation and Particles Returned to Earth. *Science* 375: 1011–16.

Takir, D., Emery, J. P., Mcsween, J. H. Y., Hibbitts, C. A., Clark, R. N., Pearson, N., and Wang, A. 2013. Nature and Degree of Aqueous Alteration in CM and CI Carbonaceous Chondrites. *Meteoritics & Planetary Science* 48: 1618–37.

Tomeoka, K., and Buseck, P. R. 1985. Indicators of Aqueous Alteration in CM Carbonaceous Chondrites: Microtextures of a Layered Mineral Containing Fe, S, O and Ni. *Geochimica et Cosmochimica Acta* 49: 2149–63.

Tomeoka, K., and Buseck, P. R. 1988. Matrix Mineralogy of the Orgueil CI Carbonaceous Chondrite. *Geochimica et Cosmochimica Acta* 52: 1627–40.

Tomeoka, K., Mcsween, H. Y., and Buseck, P. R. 1989. Mineralogical Alteration of CM Carbonaceous Chondrites: A Review. *Proceedings of the NIPR Symposium on Antarctic Meteorites* 2: 221–234.

Uesugi, F., Koshiya, S., Kikkawa, J., Nagai, T., Mitsuishi, K., and Kimoto, K. 2021. Non-negative Matrix Factorization for Mining Big Data Obtained using Four-dimensional Scanning Transmission Electron Microscopy. *Ultramicroscopy* 221: 113–168.

Vacher, L. G., Truche, L., Faure, F., Tissandier, L., Mosser-Ruck, R., and Marrocchi, Y. 2019. Deciphering the Conditions of Tochilinite and Cronstedtite Formation in CM Chondrites from Low Temperature Hydrothermal Experiments. *Meteoritics & Planetary Science* 54: 1870–89.

Velbel, M. A., and Palmer, E. E. 2011. Fine-Grained Serpentine in CM2 Carbonaceous Chondrites and its Implications for the Extent of Aqueous Alteration on the Parent Body: A Review. *Clays and Clay Minerals* 59: 416–432.

Viennet, J. C., Roskosz, M., Nakamura, T., Beck, P., Baptiste, B., Lavina, B., Alp, E. E., Hu, M. Y., et al. 2023. Interaction between Clay Minerals and Organics in Asteroid Ryugu. *Geochemical Perspectives Letters* 25: 8–12.

Wang, Y. 2021. The Chromophore Fading and Spectroscopy Analysis of Lazurite in Annealing Treatment. *Spectrochimica Acta Part A: Molecular and Biomolecular Spectroscopy* 247: 119117.

Wang, Y., He, J., Meng, X., Duan, Z., Li, Y., Zhou, F., Zhao, L., Zhang, P., Su, Q., and Pang, S. 2020. A Simple Construction Strategy for Fabrication of Sulfur-Doped Silicate Materials from Attapulgite. *New Journal of Chemistry* 44: 401–414.

Wilke, M., Jugo, P. J., Klimm, K., Susini, J., Botcharnikov, R., Kohn, S. C., and Janousch, M. 2008. The Origin of S4+ Detected in Silicate Glasses by XANES. *American Mineralogist* 93: 235–240.

Wilke, M., Klimm, K., and Kohn, S. C. 2011. Spectroscopic Studies on Sulfur Speciation in Synthetic and Natural Glasses. *Reviews in Mineralogy and Geochemistry* 73: 41–78.

Wunder, B., Deschamps, F., Watenphul, A., Guillot, S., Meixner, A., Romer, R. L., and Wirth, R. 2010. The Effect of Chrysotile Nanotubes on the Serpentine-Fluid Li-Isotopic Fractionation. *Contributions to Mineralogy and Petrology* 159: 781–790.

Yada, T., Abe, M., Okada, T., Nakato, A., Yogata, K., Miyazaki, A., Hatakeda, K., et al. 2022. Preliminary Analysis of the Hayabusa2 Samples Returned from C-Type Asteroid Ryugu. *Nature Astronomy* 6: 214–220.

Yamaguchi, A., Tomioka, N., Ito, M., Shirai, N., Kimura, M., Greenwood, R. C., Liu, M.-C., McCain, K. A., et al.

2023. Insight into Multi-Step Geological Evolution of C-Type Asteroids from Ryugu Particles. *Nature Astronomy* 7: 398–405.

Yokoyama, T., Nagashima, K., Nakai, I., Young, E. D., Abe, Y., Aléon, J., Alexander, C. M. O. D., Amari, S., et al. 2023. Samples Returned from the Asteroid Ryugu Are Similar to Ivuna-Type Carbonaceous Meteorites. *Science* 379: eabn7850.

Yoshimura, T., Takano, Y., Naraoka, H., Koga, T., Araoka, D., Ogawa, N. O., Schmitt-Kopplin, P., et al. 2023. Chemical Evolution of Primordial Salts and Organic Sulfur Molecules in the Asteroid 162173 Ryugu. *Nature Communications* 14: 5284.

Zega, T. J., and Buseck, P. R. 2003. Fine-Grained-Rim Mineralogy of the Cold Bokkeveld CM Chondrite. *Geochimica et Cosmochimica Acta* 67: 1711–21.

Zega, T. J., Garvie, L. A. J., Dódony, I., and Buseck, P. R. 2004. Serpentine Nanotubes in the Mighei CM Chondrite. *Earth and Planetary Science Letters* 223: 141–46.

Zega, T. J., Garvie, L. A. J., Dódony, I., Friedrich, H., Stroud, R. M., and Buseck, P. R. 2006. Polyhedral Serpentine Grains in CM Chondrites. *Meteoritics & Planetary Science* 41: 681–88.

Zolensky, M. E. 1984. Hydrothermal alteration of CM carbonaceous chondrites: Implications of the identification of tochilinite as one type of meteoritic PCP. *Meteoritics*, 19: 346–47.

Zolensky, M., Barrett, R., and Browning, L. 1993. Mineralogy and Composition of Matrix and Chondrule Rims in Carbonaceous Chondrites. *Geochimica et Cosmochimica Acta* 57: 3123–48.

Zolensky, M. E., Mittlefehldt, D. W., Lipschutz, M. E., Wang, M.-S., Clayton, R. N., Mayeda, T. K., Grady, M. M., Pillinger, C., and B, D. 1997. CM Chondrites Exhibit the Complete Petrologic Range from Type 2 to 1. *Geochimica et Cosmochimica Acta* 61: 5099–5115.

Zolotov, M. Y. 2016. Formation of Sulfates on Parent Bodies of Carbonaceous Chondrites, Ceres, Europa, and Other Icy Bodies 47th Lunar and Planetary Science Conference, abstract #1778. Lunar and Planetary Institute Houston.

SUPPORTING INFORMATION

Additional supporting information may be found in the online version of this article.

Figure S1. SEM backscatter images showing selected features in Winchcombe CM2 (P30453), with points (a–f) measured for SEM–EDX and Fe-K XANES (right) highlighted. A stack of baseline subtracted Fe-K XANES $1s \rightarrow 3d$ pre-edge centroids (right) for ferrous (Fe^{2+}) and ferric (Fe^{3+}) Fe-silicate references, San Carlos olivine and nontronite (NG-1), respectively, compared to the Fe-silicates (a–e) and Fe-sulfide-hydroxide (f) features observed in Winchcombe (P30453). $Fe^{3+}/\Sigma Fe$ values are estimated for Fe-silicates only (see Table S2 for Fe-K XANES pre-edge centroid and absorption edge values).

Table S2. Fe-K XANES $1s \rightarrow 3d$ pre-edge and absorption edge for Winchcombe olivine (a), Fe-silicate clay features (b–e) and Fe-sulfide-hydroxide (f), with estimations of $Fe^{3+}/\Sigma Fe$. The reference minerals (below) include the experiment estimations of $Fe^{3+}/\Sigma Fe$ with the theoretical values.

Figure S2. Plot of SO_3 equiv. in oxide wt% equivalent against lattice spacings measured using HRTEM in the Winchcombe site B lamella. The sites taken for STEM-EDS measurements are the same sites where lattice spacing measurements were taken. The plot shows a clear anti-correlation between these two parameters, with $R = -0.96$. It should be noted that this is a preliminary suggestion of a relationship between these two parameters, and further work is needed to investigate whether the same is true for other sites in Winchcombe and for other samples.

Table S3. Normalized TEM-EDS compositions of representative serpentine and S-serpentine phases.

Table S4. Normalized compositions acquired from correlative EDS measurements and the respective loading vectors (LV).

Figure S3. Full non-negative matrix factorization (NMF) results using 20 loading vectors (LVs) in the segmentation of 4D STEM data from Winchcombe site B lamella. Virtual bright-field (vBF) images are shown with the corresponding phase maps (produced by each loading vector) plotted on top, along with the corresponding 1D averaged radial variance profile plots (RVPs), and the original loading vector RVPs. The peaks are annotated with their respective d-spacings. All maps are displayed with normalized intensity. Differences seen between the averaged RVPs and the original loading vector RVPs are due to normalization of the data for the averaged RVPs. This makes all features of the original LV plots relatively comparable with each other, meaning that even small features are augmented. Aside from the characteristic serpentine reflections at ~0.70 nm (7 Å) seen in LVs 3, 5, 9, 14, 20 (7.44, 7.02, 7.44, 7.02 and 7.33 Å, respectively), other reflections that appear in nearly every LV plot correspond to the 100, 002 and 111 planes (averages of 4.60, 3.70 and 2.55 Å, respectively). Two exceptions are LVs 4 and 16, which are missing peaks at ~2.55 Å (111 plane); however, they do have reflections at 2.64 Å, corresponding to the 110 plane of serpentine. The diagonal features seen in LVs 1, 12 and 15 are likely due to variations in sample thickness resulting from FIB milling. All comparisons and identifications made using data compiled from Mellini (1982), Brindley and Brown (1984); Mellini and Cressey (2010); Hicks et al. (2014); Viennet et al. (2023).